POLITECNICO DI TORINO
Repository ISTITUZIONALE

Ultrasound-responsive nutlin-loaded nanoparticles for combined chemotherapy and piezoelectric treatment of glioblastoma cells

Original
Ultrasound-responsive nutlin-loaded nanoparticles for combined chemotherapy and piezoelectric treatment of glioblastoma cells / Pucci, C.; Marino, A.; Sen, O.; De Pasquale, D.; Bartolucci, M.; Iturrioz-Rodriguez, N.; di Leo, N.; de Vito, G.; Debellis, D.; Petretto, A.; Ciofani, G.. - In: ACTA BIOMATERIALIA. - ISSN 1742-7061. - STAMPA. - 139:(2022), pp. 218-236. [10.1016/j.actbio.2021.04.005]

Availability:
This version is available at: 11583/2954696 since: 2022-02-04T16:03:48Z

Publisher:
Elsevier

Published
DOI:10.1016/j.actbio.2021.04.005

Terms of use:

This article is made available under terms and conditions as specified in the corresponding bibliographic description in the repository

Publisher copyright

(Article begins on next page)

12 October 2024

Acta Biomaterialia 139 (2022) 218–236

Contents lists available at ScienceDirect

Acta Biomaterialia

journal homepage: www.elsevier.com/locate/actbio

Full length article

Ultrasound-responsive nutlin-loaded nanoparticles for combined chemotherapy and piezoelectric treatment of glioblastoma cells☆

Carlotta Pucci[a,1,*], Attilio Marino[a,1,*], Özlem Şen[a,1], Daniele De Pasquale[a,b], Martina Bartolucci[c], Nerea Iturrioz-Rodríguez[a], Nicoletta di Leo[a,b], Giuseppe de Vito[d,e], Doriana Debellis[f], Andrea Petretto[c], Gianni Ciofani[a,*]

[a] Istituto Italiano di Tecnologia, Smart Bio-Interfaces, Viale Rinaldo Piaggio 34, 56025 Pontedera, Italy
[b] Scuola Superiore Sant'Anna, The Biorobotics Institute, Viale Rinaldo Piaggio 34, 56025 Pontedera, Italy
[c] IRCCS Istituto Giannina Gaslini, Via Gerolamo Gaslini 5, 16147 Genova, Italy
[d] University of Florence, Department of Neuroscience, Psychology, Drug Research and Child Health, Viale Gaetano Pieraccini 6, 50139 Florence, Italy
[e] European Laboratory for Non-Linear Spectroscopy, Via Nello Carrara 1, 50019 Sesto Fiorentino, Italy
[f] Istituto Italiano di Tecnologia, Electron Microscopy Facility, Via Morego 30, 16163 Genova, Italy

ARTICLE INFO

Article history:
Received 8 February 2021
Revised 16 March 2021
Accepted 6 April 2021
Available online 21 April 2021

Keywords:
Piezoelectric nanoparticles
Nutlin-3a
Ultrasound
Glioblastoma
Drug resistance

ABSTRACT

Glioblastoma multiforme (GBM), also known as grade IV astrocytoma, represents the most aggressive primary brain tumor. The complex genetic heterogeneity, the acquired drug resistance, and the presence of the blood-brain barrier (BBB) limit the efficacy of the current therapies, with effectiveness demonstrated only in a small subset of patients. To overcome these issues, here we propose an anticancer approach based on ultrasound-responsive drug-loaded organic piezoelectric nanoparticles. This anticancer nanoplatform consists of nutlin-3a-loaded ApoE-functionalized P(VDF-TrFE) nanoparticles, that can be remotely activated with ultrasound-based mechanical stimulations to induce drug release and to locally deliver anticancer electric cues. The combination of chemotherapy treatment with chronic piezoelectric stimulation resulted in activation of cell apoptosis and anti-proliferation pathways, induction of cell necrosis, inhibition of cancer migration, and reduction of cell invasiveness in drug-resistant GBM cells. Obtained results pave the way for the use of innovative multifunctional nanomaterials in less invasive and more focused anticancer treatments, able to reduce drug resistance in GBM.

Statement of significance

Piezoelectric hybrid lipid-polymeric nanoparticles, efficiently encapsulating a non-genotoxic drug (nutlin-3a) and functionalized with a peptide (ApoE) that enhances their passage through the BBB, are proposed. Upon ultrasound stimulation, nanovectors resulted able to reduce cell migration, actin polymerization, and invasion ability of glioma cells, while fostering apoptotic and necrotic events. This wireless activation of anticancer action paves the way to a less invasive, more focused and efficient therapeutic strategy.

© 2021 The Authors. Published by Elsevier Ltd on behalf of Acta Materialia Inc.
This is an open access article under the CC BY-NC-ND license
(http://creativecommons.org/licenses/by-nc-nd/4.0/)

1. Introduction

Glioblastoma multiforme (GBM) is one of the deadliest brain tumors, with a median survival rate of 12 – 15 months and a 5-years survival percentage of about 5% [1]. The gold-standard treatment for GBM combines surgical resection, radiotherapy, and chemotherapy. Nevertheless, currently available therapeutic approaches are extremely inefficient and they only marginally improve the average patient survival [2–4]. Despite the extraordinary effort put into

☆ Part of the Special Issue on Conductive and Electroactive Biomaterials and Bioelectronics, guest-edited by Professors Jonathan Rivnay and Mehdi Nikkhah.

* Corresponding author.
E-mail addresses: carlotta.pucci@iit.it (C. Pucci), attilio.marino@iit.it (A. Marino), gianni.ciofani@iit.it (G. Ciofani).

[1] These authors equally contributed to this work

https://doi.org/10.1016/j.actbio.2021.04.005
1742-7061/© 2021 The Authors. Published by Elsevier Ltd on behalf of Acta Materialia Inc. This is an open access article under the CC BY-NC-ND license (http://creativecommons.org/licenses/by-nc-nd/4.0/)

finding effective therapeutic strategies, the prognosis for GBM is, at the moment, still very poor. The difficulties in treating GBM arise from its particularly complex and diffuse nature, its invasiveness, and its high genetic heterogeneity [5]. Moreover, the presence of the blood-brain barrier (BBB) prevents most of the drugs from reaching the tumor site [6]; furthermore, the efficacy of the drug treatments able to cross BBB and target the tumor is also limited by the drug resistance mechanisms developed by GBM [7].

Over the past decades, nanotechnology offered effective solutions for the treatment of disparate pathologies owing to the possibilities to improve the systemic delivery of drugs and to enhance their bioavailability [8,9]. Moreover, nanoparticles can be engineered to selectively target specific cellular receptors that could enhance their uptake or favor their permeation through the BBB [10]. Active targeting can be achieved by means of different kinds of ligands, but peptides seem to be the most promising due to their stability, low immunogenicity, and easy production [8,11].

An innovative paradigm in cancer nanomedicine regards the development of active nanodevices/nanotransducers able to remotely respond to external stimuli (*e.g.*, magnetic fields, light irradiation and ultrasound, among others), and to convert different forms of energy into physical/chemical anticancer cues (*e.g.*, heat, reactive oxygen species, electric cues) [12–15]. In this regard, piezoelectric nanomaterials represent a promising platform for the non-invasive and remote delivery of local electric cues to cells and tissues [16–19]. As a result of the direct piezoelectric effect, these nanotransducers generate electric potentials on their surface in response to mechanical deformations, a phenomenon named mechano-electric transduction. The remote mechanical activation of these materials can be achieved in a non-harmful way by using ultrasounds (US); in the context of cancer therapy, our group demonstrated for the first time the local delivery of anticancer electric cues by using piezoelectric barium titanate nanoparticles in breast cancer [20] and glioblastoma [15] cells. This stimulation approach is similar to that one of the tumor-treating fields [21,22], but it is local and can be specifically targeted to malignant cells, therefore avoiding side effects in healthy tissues/cells (*e.g.*, inhibition of astrocyte proliferation [23]). Chronic piezoelectric stimulation was proven to reduce drug resistance and to inhibit cell proliferation by interfering with Ca^{2+} and K^{+} homeostasis, and by affecting the organization of mitotic spindles during mitosis [15,20].

Inorganic piezoelectric materials such as barium titanate or zinc oxide have high piezoelectric coefficients, but they raise some concerns about biocompatibility and biodegradability *in vivo* [24]. On the other hand, despite their slightly lower piezoelectric performances, organic piezoelectric polymers such as poly(vinylidene fluoride) -PVDF- and its copolymer poly(vinylidene fluoride-trifluoro ethylene) -P(VDF-TrFE)- represent a valid alternative thanks to their biocompatibility and easier tunability and processing [24]. Pure or composite P(VDF-TrFE) films and scaffolds were previously shown to successfully induce cell stimulation and differentiation, in combination with an appropriate US stimulus [25–27]. The grand challenge in organic piezoelectric nanomaterial development is the ability to self-assemble them in small organic nanoparticles while keeping their piezoelectric outputs, without recurring to other inorganic materials to improve the performances. Currently, just two examples can be found in the literature. Xiao *et al.* successfully implemented a straightforward formulation protocol to produce small nanoparticles of P(VDF-TrFE) mainly arranged in the piezoelectric β-phase [28]. These nanoparticles have been exploited in ferroelectric organic photovoltaic devices and no biological applications were envisaged. More recently, Ma *et al.* proposed nylon-11 nanoparticles for stem cell osteogenic differentiation upon US exposure [18]. It appears clear, thus, that this research area is still at its very dawn, despite the enormous impact that piezoelectric organic nanoparticles could have in several technological applications and, as previously shown, in cancer therapy.

In this context, our work aims at providing hybrid lipid-polymer nanocarriers, consisting of a piezoelectric polymeric core and a shell of biocompatible and easily modifiable lipids. Hybrid lipid-polymer nanoparticles combine the advantages of polymeric nanoparticles (structural integrity, superior stability and controlled drug release) and liposomes (higher biocompatibility and biomimetic activity) for an improved therapeutic outcome [29]. Our final piezoelectric nanoparticles, here called PNPs, were composed of a core of P(VDF-TrFE), crystallized mainly in its β-phase, and encapsulating the drug nutlin-3a (Nut), an antagonist of the murine double minute-2 (MDM2) protein, which is a negative regulator of the tumor suppressor protein p53 [30,31]. The polymeric core is surrounded by a shell of 1,2-distearoyl-*sn*-glycero-3-phosphoethanolamine-N-[amino(polyethylene glycol)] (DSPE-PEG), functionalized with a peptide derived from the specific amino acid sequence of the apolipoprotein E (ApoE) that binds to the low-density lipoprotein receptor (LDLr) of capillary endothelial cells [32]. LDLrs are overexpressed in brain endothelial cells and, therefore, the ApoE-derived peptide should enhance PNP passage through the BBB by transcytosis [33]; moreover, since some LDLrs are also overexpressed in glioblastoma cells, ApoE can potentially favor tumor targeting [34]. In fact, it has been demonstrated that apolipoprotein E is involved in lipid trafficking within tumors, especially in rapidly growing tumors such as a glioblastoma, making ApoE an interesting potential mediator of GBM targeting [35].

The main goal of this work was to develop an innovative nanotechnology-based anticancer approach to counteract the growth of GBM. The innovative solution mainly consists of a platform based on Nut-loaded ApoE-functionalized P(VDF-TrFE) nanoparticles (PNPs) able to cross the BBB, release the chemotherapy drug, and deliver anticancer electric stimulations to GBM cells. For the first time in the literature, we fabricated, characterized and finally tested the potential of such nanoplatform in relevant *in vitro* models. After demonstrating the ability of the nanomaterial to cross the BBB in biomimetic dynamic multicellular models, the anticancer potential of the piezoelectric stimulation in combination with the chemotherapy treatment was investigated in terms of apoptosis/necrosis, cell migration, actin polymerization, cell invasiveness, and proteomics in Nut-resistant GBM cells.

2. Materials and methods

2.1. Nanoparticles synthesis

Hybrid lipid-polymeric piezoelectric nanoparticles were synthesized by following a procedure adapted from a previous work by Xiao *et al.* [28]. Briefly, 2 mL of P(VDF-TrFE) (45:65, Piezotech) (5 mg/mL) and 200 µL of a solution of nutlin-3a (Nut, 5 mg/mL, Sigma Aldrich) in acetone (Sigma Aldrich) were quickly injected with a syringe into 4.5 mL of an aqueous dispersion containing DSPE-PEG (1 mg/mL, Nanocs) under vigorous stirring. The above mixture was sonicated for 10 min in an ice bath (amplitude 70%) using an ultrasonic tip (Fisherbrand™ Q125 Sonicator), and then let under agitation for a few hours to evaporate the majority of the organic solvent. Afterward, the mixture was purified with Amicon® centrifuge filters (Ultra-4 Centrifugal Filter Unit [MWCO 100 kDa], Sigma-Aldrich) at 2460 *g* for 15 min at 15°C. The process was repeated three times, and each time the pellet was redispersed in 4 mL sterile MilliQ water.

The recrystallization of the polymeric core was performed by refluxing the nanoparticles at 90°C, above the Curie temperature of P(VDF-TrFE), for 60 min, and then cooling down to room temperature at 1°C/min. At the end of the reflux procedure, a total of 1 mg DSPE-PEG or DSPE-PEG/DSPE-PEG-maleimide (1/1) was added

to further stabilize the nanoparticles, subsequently sonicated for 10 min (amplitude 70%) using an ultrasonic tip (Fisherbrand™ Q125 Sonicator). The lipid in excess was removed by three centrifugation steps with Amicon® centrifuge filters (Ultra-4 Centrifugal Filter Unit [MWCO 100 kDa], Sigma-Aldrich) at 2460 *g* for 15 min at 15°C.

For the functionalization, 200 µL of a 2 mg/mL aqueous solution of a peptide corresponding to the 141-150 residues of apolipoprotein E (ApoE) (GenScript) were added to 4 mL of the nanoparticles (2 mg/mL), and let under agitation at 4°C for 4 h. Thereafter, functionalized P(VDF-TrFE) nanoparticles (PNPs) were centrifuged 3 times with Amicon® centrifuge filters (Ultra-4 Centrifugal Filter Unit [MWCO 100 kDa], Sigma-Aldrich) at 2460 *g* for 15 min at 15°C to remove unreacted peptide chains.

Empty nanoparticles were prepared following the same protocol, without dissolving nutlin-3a in the initial polymer/acetone solution.

Fluorescent nanoparticles were prepared in the same way, but adding 5 µL of fluorescent Vybrant™ DiO cell-labeling dye (Invitrogen) to the 2 mL polymer/acetone solution before mixing it with the lipid aqueous dispersion.

2.2. Electron microscopy

Scanning electron microscopy (SEM) analysis was performed with a Helios NanoLab 600i FIB/SEM, FEI. A drop of the sample at a concentration of 70 µg/mL was cast on a silicon wafer and let to dry overnight. Thereafter, the sample was gold-sputtered with a Quorum Tech Q150RES Gold Sputter Coater with 30 mA for 60 s before the imaging. The morphology and the size of the nanoparticles were evaluated by transmission electron microscopy (TEM). Samples at a concentration of 50 µg/mL were sonicated for 2 min. A drop of the sample was deposited on a Cu grid (150 mesh) coated with an ultrathin amorphous carbon film. TEM analyses were carried out with a JEOL 1011 operated at 100 kV. Annular dark-field (ADF) scanning transmission electron microscopy (STEM) was performed using a JEOL JEM-1400Plus transmission electron microscope with a LaB_6 thermionic source, operated at 120 kV using a double-tilt analytical holder. Energy-dispersive X-ray (EDS) analyses have been carried out using a JEOL Dry SD30GV silicon-drift detector (SDD), with a 30 mm^2 effective area.

The size of the nanoparticles was inferred by measuring their diameter in several SEM and TEM images with ImageJ. Then, a statistical analysis was performed to compute the frequency count with OriginPro 9.1; the same software was used to fit these data with a LogNormal distribution.

2.3. Dynamic light scattering and ζ-potential measurements

The hydrodynamic diameter and ζ-potential of non-functionalized plain PNPs and PNPs were evaluated with a Zeta-sizer NanoZS90 (Malvern Instruments Ltd). Measurements were performed on dispersions at a concentration of 500 μg/mL at 37°C. The hydrodynamic diameter was measured at pH 4.5 (in phosphate buffer), at pH 7.4 (in phosphate-buffered saline solution, PBS, Sigma-Aldrich), and in Dulbecco's modified Eagle's medium (DMEM, Sigma-Aldrich) with 10% fetal bovine serum (FBS, Sigma-Aldrich). All of these conditions were studied with or without H_2O_2 (100 µM), used to simulate oxidative stress conditions. The ζ-potential was measured only in ultrapure MilliQ water. The software uses the CONTIN analysis to derive the intensity distribution and the cumulant analysis to obtain the hydrodynamic diameter and the polydispersity index.

2.4. Fourier-transformed infrared and Raman spectroscopy

Fourier-transformed infrared (FTIR) spectroscopy was performed to highlight the characteristic peaks of P(VDF-TrFE) and plain PNPs using a Shimadzu Miracle 10 on freeze-dried samples. Spectra were collected in the range of 450 – 1500 cm^{-1} with a resolution of 2 cm^{-1} and are the average result of 16 scans.

The fraction of P(VDF-TrFE) in the β-phase, $F(\beta)$, with respect to the α-phase, was evaluated by comparing the intensity of the characteristic peaks of the two phases (765 cm^{-1} for the β-phase and 840 $cm^{-1}$for the α-phase) using the formula [36,37]:

$$F(\beta) = \frac{A_\beta}{\left(\frac{K_\beta}{K_\alpha}\right)A_\alpha + A_\beta}$$

where A_α and A_β represent the absorbance at 765 and 840 cm^{-1}, respectively, while K_α and K_β are the corresponding absorption coefficients ($K_\alpha = 6.1 \cdot 10^4$ cm^2/mol and $K_\beta = 7.7 \cdot 10^4$ cm^2/mol) [38].

Raman spectroscopy (LabRAM HR Evolution; Horiba) was first performed to analyze the crystalline structure of both P(VDF-TrFE) alone and in plain PNPs; an estimate of β-phase content with respect to the α-phase (β/α) was obtained by dividing the intensity of the Raman peak at 848 cm^{-1}, corresponding to the β-phase (I_β), by the intensity of the Raman peak at 803 cm^{-1}, corresponding to the α-phase (I_α), as reported in the literature [38].

2.5. Thermogravimetric analysis and differential scanning calorimetry

Thermogravimetric analysis (TGA) was carried out to determine the percentage of each component (namely, P(VDF-TrFE) and DSPE-PEG) in plain PNPs with a Q500 analyzer (TA Instrument), by heating the samples from 30 to 700°C at a heating rate of 5°C/min under nitrogen atmosphere (flow rate of 50 mL/min).

Differential scanning calorimetry (DSC) curves were obtained using a DSC-1 STARe System (Mettler Toledo) to obtain information regarding the thermal behavior of P(VDF-TrFE), DSPE-PEG, and plain PNPs. The DSC analysis has been performed on 1 mg of freeze-dried samples from 20 to 200°C at a heating rate of 10°C/min. The reported thermograms represent the first heating ramp to portray the crystallinity of the obtained nanoparticles, avoiding the reorganization in bigger aggregates due to the melting phenomenon that could result into the second heating ramp.

2.6. Functionalization assessment

The presence of the ApoE peptide on the surface of the nanoparticles was evaluated by fluorescence spectroscopy, exploiting the fluorescence of the tryptophan residue in the peptide [32]. A Cary Eclipse fluorescence spectrofluorimeter (Agilent Technologies) was used to measure the emission signal in the range 300 – 440 nm, after excitation at 280 nm. The wt% of the peptide on the nanoparticles was evaluated by comparing the emission intensity at 350 nm of PNPs with a calibration curve of the free peptide in Milli-Q water. PNPs spectra were first normalized by that of the non-functionalized nanoparticles to avoid any contribution due to background scattering.

Sodium dodecyl sulfate–poly(acrylamide) gel electrophoresis (SDS-PAGE) was carried to further confirm the presence and quantify the amount of ApoE on PNPs [39]. 22.5 μL of ApoE, PNPs, or plain PNPs were mixed with 7.5 μL of Laemmli buffer (BioRad) and heated for 10 min at 95°C to favor denaturation. The samples (30 μL) were loaded into a 4–15 % Mini-PROTEAN TGX Precast Protein Gel (BioRad) previously placed in an electrophoresis

cell (Mini-PROTEAN Tetra Cell, BioRad) filled with Tris/Glycine running buffer (BioRad). A molecular weight marker (PageRuler Plus Prestained Protein Ladder, Thermo Fisher Scientific) was also run in parallel. The gel was run at 100 V for 1 h and then stained with Coomassie Blue for 1 h under agitation. The gel was then rinsed twice with a de-staining solution (10% glacial acetic acid, 40% H_2O, 50% methanol) for 20 min to remove unspecific staining, and finally washed with Milli-Q water. The bands, corresponding to the peptide, were analyzed with the software ImageJ (https://imagej.nih.gov/ij/) and the quantification was made by comparing the intensity of the bands corresponding to PNPs to those of known concentrations of plain peptide.

The ApoE amount on PNPs was also measured by BCA assay Protein Kit (Thermo Scientific). 25 μL of 16 mg/mL PNPs or plain PNPs were mixed with 200 μL of working solution. The samples were then incubated at 37°C for 30 min, and the absorbance at 560 nm of 90 μL of the samples was measured in triplicate with a VICTOR X3 (PerkinElmer) plate reader. The wt% of ApoE on the nanoparticles was evaluated by using a calibration curve of the free peptide in water (concentration range 0 – 250 μg/mL).

2.7. High-performance liquid chromatography

The loading and the release of nutlin-3a from Nut-loaded PNPs (Nut-PNPs) were quantified by high-performance liquid chromatography (HPLC) with a Shimadzu LC-20AT, using a C-18 column (150 mm × 4.6 mm i.d., 5 μm particle size). A mobile phase of 80% methanol (for HPLC, ≥ 99.9%, Sigma-Aldrich) and 20% H_2O (HPLC Plus, Sigma-Aldrich) was pumped in isocratic mode at a flow rate of 1 mL/min. The retention time of nutlin-3a was 4.77 min and its intensity was monitored by a UV detector at 260 nm.

For the drug loading quantification, 1 mg of freeze-dried Nut-PNPs were dissolved in 400 µL of acetonitrile and left in agitation at 37°C for 3 h. Afterward, 100 µL of cold ultrapure water were added and the sample centrifuged at 16000 *g* for 90 min at 4°C. The supernatant was collected and measured with HPLC. The drug loading (%) was calculated using the formula:

$$Drug\ loading\ (\%) = \frac{Nutlin\ mass\ in\ LMNVs\ (mg)}{Total\ mass\ of\ LMNVs\ (mg)} \cdot 100$$

Release studies were performed by dissolving 1 mg of Nut-PNPs either at pH 7.4 (PBS) to simulate the physiological environment or at pH 4.5 to simulate the pH of the microenvironment of cancer cells or of acidic organelles. The samples were left under agitation at 37°C and centrifuged with Amicon® centrifuge filters (Ultra-4 Centrifugal Filter Unit [MWCO 100 kDa], Sigma-Aldrich) at 2460 *g* for 15 min at 15°C at 24 and 48 h. The filtrates at the bottom of the Amicon tubes were collected and measured with HPLC to quantify the amount of nutlin-3a, whereas the pellets were re-dispersed in their buffers. To study the effect of the application of the ultrasound stimulus on the release profile, 1 mg/mL of Nut-PNPs at pH 7.4 or 4.5 were stimulated for 1 h with 1 W/cm^2 intensity and 1 MHz frequency, at 24 and 48 h time points. Single US stimuli were activated every 2 s and lasted 200 ms each (the same protocol used for the cell stimulation).

2.8. Blood-brain barrier model crossing evaluation

To evaluate the efficiency of non-functionalized plain PNPs and PNPs to cross an *in vitro* model of the BBB, an *ad hoc* bioreactor designed by our group was used [39,40]. The bioreactor in poly(methylmethacrylate) (PMMA) and poly(dimethylsiloxane) (PDMS) is composed of an upper channel (18.6 mm long, 5 mm large, and 0.5 mm high) that mimics the endothelial lumen, and of a bottom chamber (2 mm high, with a total surface of 20 mm^2), which represents the other side of the BBB (Fig. S1). The two chambers are separated by a poly(ethylene terephthalate) (PET) transparent membrane with pores of 3 µm, on top of which human endothelial cells hCMEC/D3 (Sigma-Aldrich) ($5 \cdot 10^4$ cells/cm^2) in EndoGRO-MV-VEGF medium (Merck Millipore) with 2.5% FBS and 1% penicillin-streptomycin (P/S, Gybco) were seeded, whereas the other side was populated with human brain-derived astrocytes HA (Cliniscience) ($8 \cdot 10^3$ cells/cm^2) in Astrocyte Growth Medium (Cliniscience), 1 day after hCMEC/D3 seeding. The BBB crossing experiments were performed when hCMEC/D3 formed a monolayer, which occurs after 5 days from the seeding procedure.

Transendothelial electrical resistance (TEER) measurements (with a Millipore Millicell ERS-2 Volt-Ohmmeter) were performed to check the quality of the BBB [41], whereas the apparent permeability (P_{app}) and the endothelial permeability coefficient (P_e) to a 100 μg/mL rhodamine B-dextran (70 kDa, Invitrogen) solution in complete medium were calculated as reported in the literature [42,43].

Due to the specific geometry of the upper chamber, the reproduction of the typical shear stress experienced by brain capillaries (about 10 dyn/cm^2) was guaranteed by the application of a flow of 12 mL/min [44]. A dispersion of either plain PNPs or functionalized PNPs labeled with Vybrant™ DiO in DMEM with 4.5 g/L of glucose, 5% of FBS and 5% of HEPES was perfused thanks to an Ibidi Pump for 3 h. Thereafter, the upper side of the fluidic unit was washed and left in 500 µL of the same medium used during the experiment; the medium was replaced daily for a total of 48 h. At the end of the experiment, the solution in the bottom chamber was collected and the fluorescence due to nanoparticle presence (λ_{ex} 485 nm, λ_{em} 535 nm) was measured with a VICTOR X3 plate reader (PerkinElmer). The concentration of Vybrant™ DiO-labeled nanoparticles in the lower chamber of the fluidic unit was evaluated by comparing their emission intensity with a calibration curve obtained with known concentrations of the same nanoparticles used for the experiment.

Images of the BBB model were obtained by C2s confocal microscope (Nikon). Briefly, at the end of the experiment, the BBBs treated with nanoparticles were fixed with 4% paraformaldehyde (PFA) for 20 min, washed, and stained with TRITC-phalloidin (1:100, Sigma-Aldrich) and Hoechst 33342 (1:1000, Invitrogen) for 2 h.

2.9. Drug and nanoparticle testing in glioblastoma cell lines

T98G (ATCC® CRL-1690™), U251 MG (Merck), and U87 MG (ATCC® HTB-14™) glioblastoma cell lines were cultured in T75 flasks with DMEM, supplemented with 10% FBS (Gibco), 100 IU/mL penicillin (Gibco), and 100 μg/mL streptomycin (Gibco). Cells were cultured by keeping a 20-85% confluency range and then seeded in 24 multiwell at a density of $2 \cdot 10^4$ cells/cm^2 for drug and nanoparticle testing. Concerning Nut treatment, the effect of different drug concentrations (0.2, 1.0, 5.0, 25.0 µM; 48 h incubation) and of the vehicle (dimethylsulfoxide -DMSO-, 1:185 dilution in the complete medium; 48 h incubation) on cell metabolism has been analyzed by using the WST-1 Assay Reagent (2-(4-iodophenyl)-3-(4-nitrophenyl)-5-(2,4-disulfophenyl)-2H-tetrazolium sodium salt; BioVision), similarly as previously described [45]. Briefly, cultures were rinsed with PBS and then incubated with the WST-1 reagent (1:11 dilution in phenol red-free complete medium for 45 min at 37°C). At the end of the reagent incubation, supernatants were collected and absorbance was measured at 450 nm with a Perkin Elmer VICTOR X3 UV-Vis spectrophotometer. The absorbance of the plain phenol red-free medium (blank) was subtracted from measurements. Finally, absorbance data were normalized to the non-treated controls. Following the same experimental procedures, the toxicity of PNPs and Nut-PNPs (100,

250, 500, 1000 μg/mL; 48 h incubation) has been assessed. Since the most interesting results were found in T98G cells -this cell line was found to be resistant to free-Nut but sensitive to Nut-PNPs-, the following investigations have been carried out on these cells.

2.10. Nanoparticle internalization: Confocal fluorescence and Raman imaging

For confocal fluorescence microscopy imaging, T98G cells were seeded on μ-Plate 24 Well (Ibidi, seeding density of $2 \cdot 10^4$ cells/cm^2). At 12 h from seeding, cells were incubated for 24 and 72 h with 500 μg/mL Vybrant™ DiO-labeled PNPs and then fixed with 4% PFA in PBS for 20 min at 4°C. Cultures were then stained with TRITC-phalloidin (1:100 in PBS, Sigma-Aldrich) and Hoechst 33342 (1:1000 in PBS, Invitrogen) for 2 h. Samples were finally rinsed with PBS and imaged with a C2s confocal microscope (Nikon). 3D image reconstruction was finally performed by using NIS Elements Software (Nikon).

Concerning confocal Raman imaging, T98G cells were seeded on Raman grade calcium fluoride substrates (Crystran, seeding density $2 \cdot 10^4$ cells/cm^2). At 12 h from seeding, cells were incubated for 24 h with 500 μg/mL PNPs and then fixed with 4% PFA in PBS for 20 min at 4°C. Cultures were dehydrated and then imaged with a confocal Raman microscope (LabRAM HR Evolution, Horiba). LabSpec 6 software has been used to obtain the signal maps; signals of the PNPs (β-phase: 820 cm^{-1} > Raman shift > 880 cm^{-1}), cell proteins (amide I region [46]: 1600 cm^{-1} > Raman shift > 1700 cm^{-1}), and nuclei (DNA [47,48]: 760 cm^{-1} > Raman shift > 790 cm^{-1}) were used, with a pixel intensity proportional to the integrated peak area.

2.11. Calcium imaging during piezoelectric stimulation

T98G cells were seeded on WillCo-dish® glass bottom dishes (seeding density $2 \cdot 10^4$ cells/cm^2). At 12 h from seeding, cells were incubated for 24 h with 500 μg/mL PNPs. Before imaging, cells were incubated with Fluo-4 AM (Invitrogen; 1 μM in DMEM, 30 min incubation at 37°C) and then the solution was replaced with phenol red-free DMEM supplemented with HEPES (Thermo Fisher). Time-lapse imaging was carried out with a confocal laser scanning microscopy (C2s confocal microscope, Nikon) by using a perfect focus system (Nikon). Before starting the stimulation, cells were maintained for 20 min to complete the de-esterification of the AM groups of the fluorescent dye. During Ca^{2+} imaging, US were generated by a KTAC-4000 device (Sonidel) equipped with a S-PW 3 mm diameter tip. Chronic US stimulation was performed following a previously described protocol, which is known to activate piezoelectric nanoparticles without inducing detectable temperature increases of the cell medium [15,49]. Briefly, trains of US were delivered with 1 W/cm^2 intensity and 1 MHz frequency. US were delivered starting at t = 500 s of the time-lapse imaging. Single stimuli were activated every 2 s and lasted 200 ms each.

Fluorescence intensities (F) were calculated as the mean pixel value in the intracellular region of interest (ROI), once subtracted the extracellular background. The fluorescence intensity at time t = 0 s was indicated as F_0; The F/F_0 trace of the cells incubated with PNPs and stimulated with US (PNPs + US) was reported in a graph and compared to that one of cultures stimulated with US without the presence of nanoparticles (US). Representative F/F_0 images at t = 8 min, t = 33 min, t = 60 min, and t = 85 min of the time-lapse Ca^{2+} imaging were obtained with ImageJ software by using the divide function of the Math process after background subtraction, as previously described [20].

2.12. Investigations on cell apoptosis and necrosis

T98G cells were seeded in 24 multiwell at a density of $2 \cdot 10^4$ cells/cm^2. At 12 h from seeding, cultures were organized in 8 experimental classes: controls without (Control) or with (Control + US) US stimulation, cells incubated with free Nut without (Nut) or with (Nut + US) US stimulation, cells incubated with PNPs without (PNPs) or with (PNPs + US) US stimulation, and cells incubated with Nut-PNPs without (Nut-PNPs) or with (Nut-PNPs + US) US stimulation. Both PNPs and Nut-PNPs were used at 500 μg/mL; concerning the Nut and Nut + US experimental classes, the free drug was at concentration 21.5 μM, which corresponds to the amount of Nut loaded in 500 μg/mL of Nut-PNPs. US were delivered following the stimulation protocol described above in section 2.11, 1 h per day for 2 days.

After 12 h, samples were washed in PBS, treated with trypsin for 5 min at 37°C, centrifuged, and finally resuspended in the 1 × annexin V binding buffer supplemented with 1 μg/mL of propidium iodide (PI) and 2.5 μM annexin V-FITC (15 min at 37°C). The suspension of stained cells was then analyzed by flow cytometry as previously described [50]. Specifically, the fluorescence intensity of the cells was measured with a Beckman Coulter CytoFLEX (for annexin V-FITC: λ_{ex} 488 nm, λ_{em} 525 ± 40 nm; for PI: λ_{ex} 488 nm, λ_{em} 690 ± 50 nm); the percentages of necrotic, late apoptotic, early apoptotic and healthy cell populations were analyzed using the CytoFLEX software.

2.13. Migration and invasion assays

A scratch assay was performed to assess the migration rate of T98G cells in the 8 previously described experimental classes (Control, Nut, PNPs, Nut-PNPs, Control + US, Nut + US, PNPs + US, Nut-PNPs + US). T98G cells were seeded in Culture Insert 2 Well systems (Ibidi) with a $5.5 \cdot 10^4$ cells/cm^2 seeding density. At 24 h from seeding, cells were incubated for 24 h with plain medium as control, 21.5 μM Nut, 500 μg/mL PNPs, or 500 μg/mL Nut-PNPs for 24 h. Thereafter, the culture inserts were removed, and the cells were washed with PBS and stained using 1 μM calcein for 15 min at 37°C (Invitrogen). Cultures were stimulated with US as reported in section 2.12. The gap between the cells (500 μm ± 100 μm) was imaged by using fluorescence microscopy (Eclipse Ti, Nikon) before starting the US stimulation protocol (t = 0 h) and after the second stimulation session (t = 24 h). The assay was performed in duplicate with three internal replicates, and at least three images were taken for each culture insert. The images were analyzed using ImageJ software using the "Wound Healing" plug-in.

To estimate the relative amounts of cellular *f*-actin and *g*-actin, T98G cells were seeded in Culture Insert 2 Well systems (Ibidi), incubated with drug/nanoparticles and stimulated with US as described above. At the end of the treatment, cells were fixed with 4% PFA at 4°C for 20 min and permeabilized with 0.1% Triton X-100 (Sigma) for 15 min. *f*-actin, *g*-actin and nuclei were labeled with TRITC-phalloidin (1:200), deoxyribonuclease I conjugate (0.3 μM, Invitrogen), and Hoechst (1:1000) at 37°C for 45 min, respectively. The images of the cells were acquired at the scratch region using confocal fluorescence microscopy. The *f*-/*g*-actin signal ratio was finally analyzed with NIS-Elements software (Nikon).

Invasion of T98G cells (in the 8 experimental conditions) was assessed *in vitro* using the Cell Invasion Assay Kit (collagen I), 24-well, 8 μm (Abcam) according to the manufacturer's protocol with some modifications. Briefly, the filter was coated using 100 μL of collagen I to form a film. 200 μL of a cell suspension ($2.3 \cdot 10^5$ T98G cells/chamber) in complete medium supplemented with drug or nanoparticles (21.5 μM Nut, 500 μg/mL PNPs, or

500 µg/mL Nut-PNPs) were added to each well of the upper chamber. 600 µL of culture medium were placed in the lower chambers. After 12 h of incubation, lower chamber media were replaced with a control invasion-inducer medium (1:10, v/v), and the cultures were stimulated with US using the same parameters described above. Cells that did not undergo invasion on the upper chamber were removed by wiping with a cotton swab. Cell dye (1:250 dilution in PBS) was incubated for 30 min in the bottom chamber and, finally, the plate was read with a VICTOR X3 (PerkinElmer) plate reader (λ_{ex} 485 nm, λ_{em} 530 nm). The fluorescence was then converted in cell number by using a standard curve.

2.14. Proteomic analysis

Samples from the 8 considered experimental classes and in experimental triplicate were lysed, reduced, and alkylated in 50 µL LYSE buffer (Preomics) at 95°C for 10 min, and sonicated with an Ultrasonic Processor UP200St (Hielscher) with 3 cycles of 30 s. Lysed samples were digested with 0.7 µg trypsin and 0.3 µg LysC overnight at 37°C. Thereafter, nanoparticles were separated from the samples centrifuging for 15 min at 18000 *g*, and samples were treated with 30 µL of 30% acetonitrile (ACN). The supernatant separated from the nanoparticles was concentrated, joined with the rest of the sample, and processed by iST protocol [51]. The resulting peptides were analyzed by a nano-UHPLC-MS/MS system using an Ultimate 3000 RSLC coupled to an Orbitrap Fusion Tribrid mass spectrometer (Thermo Scientific Instrument).

Elution was performed using a 200 cm uPAC C18 column (PharmaFluidics) mounted in the thermostated column compartment maintained at 50°C. At first, a concentration gradient from 5 to 10% buffer B (80% ACN and 20% H_2O, 5% DMSO, 0.1% FA) was applied, coupled with a flow gradient from 750 nL/min to 350 nL/min for 15 min. Then, peptides were eluted with a 60 min linear gradient from 10 to 60% of buffer B at a constant flow rate of 350 nL/min. Orbitrap detection was used for MS1 measurements at a resolving power of 120 K in a range between 375 and 1500 *m*/*z* and with a standard AGC target. Advanced peak detection was enabled for MS1 measurements. MS/MS spectra were acquired in the linear ion trap (rapid scan mode) after higher-energy C-trap dissociation (HCD) at a collision energy of 30% and with a Custom AGC target. For precursor selection, the least abundant signals in the three ranges 375-575 *m*/*z*, 574-775 *m*/*z* and 774-1500 *m*/*z* were prioritized. Dynamic Exclusion was set at 25 s.

MaxQuant software [52], version 1.6.17.0, was used to process the raw data. The false discovery rate (FDR) for the identification of proteins, peptides, and PSM (peptide-spectrum match) was set to 0.01. A minimum length of 6 amino acids was required for peptide identification. Andromeda engine, incorporated into MaxQuant software, was used to search MS/MS spectra against Uniprot human database (release UP000005640_9606 October 2020). In the processing, the variable modifications were Acetyl (Protein N-Term), Oxidation (M) and Deamidation (NQ). Carbamidomethyl (C) was selected as a fixed modification. Algorithm MaxLFQ was chosen for the protein quantification with the activated option "match between runs" to reduce the number of the missing proteins. The intensity values were extracted and statistically evaluated using the ProteinGroup Table and Perseus software version 1.6.14.0 [53]. Perseus algorithm was used to perform principal component analysis (PCA) with default parameters. The PCA of the first 2 components for all the 3 experiments was plotted. GO enrichment specific for brain tissue was obtained with the webserver HumanBase [54].

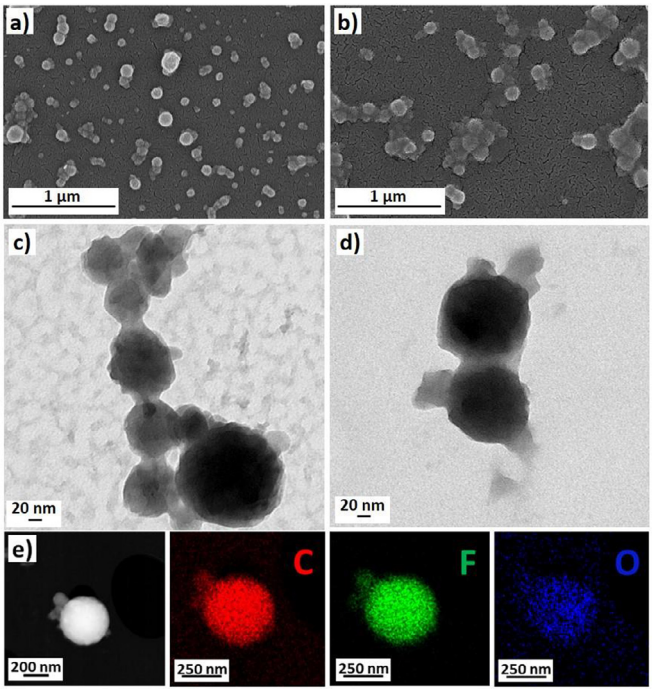

Fig. 1. Representative SEM images of a) plain and b) functionalized PNPs; representative TEM images of c) plain and d) functionalized PNPs; e) ADF/STEM image and elemental analysis (EDS) of PNPs for carbon (C, red), fluorine (F, green) and oxygen (O, blue).

2.15. Statistical analysis

Concerning BBB experiments, Student's *t*-test has been performed to compare the amount of functionalized *vs.* plain PNPs that crossed the barrier. In all other cases, ANOVA parametric test followed by Tukey's HSD *post-hoc* test was carried out for multiple distribution comparisons by using *R* software (https://www.r-project.org/).

3. Results and discussion

3.1. Physicochemical characterization of the nanoparticles

DSPE-PEG-coated P(VDF-TrFE) nanoparticles (PNPs) were synthesized following a nanoprecipitation protocol adapted from Xiao *et al* [28], and functionalized with the peptide ApoE to favor the crossing of the blood-brain barrier [32].

SEM analysis shows the formation of spherical nanoparticles with a diameter of about 92 ± 11 nm (Fig. 1a and Fig. S2a). The images also confirm that there is no significant increase in size after the functionalization of PNPs with ApoE (115 ± 20 nm; Fig. 1b and Fig. S2b). TEM analysis is in agreement with SEM imaging, showing particles with a mean diameter centered at around 89 ± 10 nm before functionalization (Fig. 1c and Fig. S2c) and at 80 ± 10 nm after functionalization (Fig. 1d and Fig. S2d). From the EDS analysis on plain PNPs (Fig. 1e and Fig. S3) it is possible to observe the presence of C, due to the backbones of both the polymer and to the DSPE-PEG, F, due to P(VDF-TrFE), and O, stemming from the DSPE-PEG. Notably, the co-localization of oxygen with carbon and fluoride confirms the successful coating of the P(VDF-TrFE) core with lipid molecules. To the best of our knowledge, this is the first example of hybrid lipid-polymeric nanoparticles prepared from the piezoelectric polymer P(VDF-TrFE). The addition of the lipid layer on the polymeric core is extremely important for biological applications, since it ensures higher biocompatibility, stealth stabil-

ity, and makes easier further functionalization with specific ligands [29].

The size of PNPs was also measured by dynamic light scattering (Fig. 2a). The intensity distribution shows a fairly monodisperse population with an average hydrodynamic diameter of 203 ± 3 nm, a polydispersity index (PdI) of 0.17 ± 0.03 and a ζ-potential of -20 ± 1 mV (Fig. 2b). The functionalization with ApoE does not significantly affect the size, the PdI, and the ζ-potential of the nanoparticles (251 ± 20 nm, 0.19 ± 0.02, and -18.1 ± 0.3 mV).

The crystalline phases of P(VDF-TrFE) confined in the core of PNPs were investigated by FTIR and Raman spectroscopy (Fig. 2c-d). Both bulk P(VDF-TrFE) and PNPs FTIR spectra present the peculiar peaks at 842 and 1279 cm^{-1}, corresponding to the β-phase of the polymer. The typical peaks of the α-phase arrangement (610, 765, 965 cm^{-1}) are very weak and extremely difficult to identify, especially for PNPs (Fig. 2c) [38]. This suggests that the polymer preferentially crystallizes in the β-phase. From the absorbance of the peaks at 765 (α-phase) and 842 cm^{-1} (β-phase), it is possible to determine the fraction $F(\beta)$ of P(VDF-TrFE) in the β-phase (see in the "Materials and Methods" section). The analysis of FTIR spectra in Fig. 2c indicates that $F(\beta)$ in the bulk polymer is around 0.7, whereas PNPs undergone the reflux procedure increases $F(\beta)$ up to 1.0, in agreement with the poor intensity of all the α-phase-related peaks in the FTIR spectra.

Raman spectroscopy (Fig. 2d) also gives useful information regarding the crystalline conformation of P(VDF-TrFE) in the nanoparticles. In fact, the α-phase has a characteristic peak at around 803 cm^{-1}, whereas the β-phase gives a peak at 848 cm^{-1}. Also in this case, from the intensities of these two contributions, it is possible to estimate the ratio between the β- and α-phase in the sample [38]. In agreement with FTIR, Raman spectroscopy highlights a significant increase of the β-phase in PNPs ($\beta/\alpha = 3$), as compared to P(VDF-TrFE) powder ($\beta/\alpha = 2$). These results confirm that the PNPs preparation protocol ensures successful recrystallization of the polymer predominantly in the β-phase, which is the most interesting phase when looking for optimal piezoelectric and ferroelectric properties [55].

As reported in literature, pure PVDF can crystallize in four different phases: α, β, δ, and γ, but it mainly assumes the non-polar α-phase when recrystallized from its melt [55–57]. In order to obtain the β-phase, PVDF needs to be mechanically stretched or poled [58,59]. The addition of TrFE to form the copolymer P(VDF-TrFE) is known to spontaneously favor the orientation in the β-phase [24]. This is in agreement with the high β-fraction observed in the bulk P(VDF-TrFE) used in this work, with a TrFE content equal to 45%. Nonetheless, as already reported by Xiao *et al.*, the nanoparticle formulation protocol and, in particular, the reflux procedure, are able to further increase the content of the β-phase, improving the piezoelectric properties of the polymer [28].

TGA analysis (Fig. 2e) shows the typical degradation temperatures of the components of plain PNPs. Bulk P(VDF-TrFE) has a distinct degradation temperature at 475°C, whereas DSPE-PEG at 380°C. In plain PNPs (Fig. 2e and Fig. S4, blue curve), the contributions of the two materials are still distinguishable, allowing to estimate that PNPs are composed of around 30% w/w of DSPE-PEG and 70% w/w of P(VDF-TrFE).

DSC thermograms of bulk P(VDF-TrFE), DSPE-PEG, and plain PNPs are reported in Fig. 2f. P(VDF-TrFE) (black line) thermogram shows the typical endothermic peak at 73°C corresponding to the transition from the ferroelectric to the paraelectric phase (Curie temperature, T_C) [60]. At higher temperatures, another endothermic peak (156°C) due to the polymer fusion ($T_{m,polymer}$) can be observed; the associated enthalpy of fusion is equal to -25 J/g, in agreement with the values reported in the literature [55]. Pure DSPE-PEG presents an endothermic peak (melting, $T_{m,lipid}$) at 59°C, mainly due to the PEG contribution, with a small shoulder at lower temperatures (around 54°C), due to DSPE; the overall enthalpy of fusion is -101 J/g [61]. In plain PNPs (blue curve), all the peaks of the individual components are still evident, with no significant shifts in the temperatures of the specific thermal events. However, the enthalpy of fusion associated with DSPE-PEG is lower in PNPs (-76 J/g), indicating a more disordered arrangement of the lipid when forming the coating around PNPs. On the other hand, the enthalpy of fusion associated with P(VDF-TrFE) is higher (-35 J/g), suggesting a higher crystallinity of the polymer after the PNPs preparation procedure.

The stability of PNPs, in terms of hydrodynamic diameter and polydispersity index, has been evaluated in different conditions (Fig. 2g-h): H_2O, PBS, PBS + H_2O_2 (100 μM), pH 4.5, pH 4.5 + H_2O_2 (100 μM), DMEM + FBS (10 %) and DMEM + FBS (10 %) + H_2O_2. The average hydrodynamic diameter of PNPs is stable in H_2O, PBS and PBS + H_2O_2 (100 μM) for at least 7 weeks after the preparation. In DMEM + FBS and DMEM + FBS + H_2O_2 the hydrodynamic diameter increases from 221 ± 9 nm and 218 ± 5 nm to 349 ± 21 and 388 ± 15 nm, respectively, after 7 weeks; a slight increase is noticeable already after 3 weeks, probably due to the formation of a protein corona around the nanoparticles that screens surface charges, reducing electrostatic repulsion and, thus, facilitating aggregation phenomena. This increment in size corresponds to an increment of the PdI (Fig. 2h) as well. Again at pH 4.5 (either with or without H_2O_2), PNPs start to form larger and more polydisperse aggregates after 3 weeks from their preparation. SEM analysis (Fig. S5) corroborates dynamic light scattering measurements, even though no evident degradation of the nanoparticles could be detected in these conditions.

The successful functionalization of PNPs with the peptide ApoE was first tested with SDS-PAGE. As shown in Fig. 3a, functionalized PNPs give rise to a band corresponding to the peptide, similarly to ApoE alone. The specificity of the method is confirmed by the absence of any detectable signal in PNPs. Comparing the intensity of the band of PNPs with that one of the peptide alone, it was estimated that ApoE accounts for the 1.6 ± 2 wt% of the nanoparticles. Fluorescence spectroscopy has been used to confirm the presence ApoE, by exploiting its fluorescence similarly to what already done in previous reports [32,39]. PNPs and the peptide alone show a typical fluorescence emission at 350 nm; on the other hand, plain PNPs do not show appreciable fluorescence (Fig. 3b). By comparing the emission intensity of functionalized PNPs to a calibration curve obtained with different concentrations of the free peptide, the wt% of the peptide bound to the surface of the nanoparticles was found to be 1.7 ± 0.5. Finally, the functionalization was also quantified to be 1.1 ± 0.7 wt% with the BCA assay. The amounts of ApoE in PNPs determined with these different techniques are in quite good agreement; considering the nanoparticle size (from SEM and TEM analysis), the density of ApoE molecules on PNPs surface was found to be 0.2 – 0.1 peptide/nm^2, in agreement with values found in the literature [39,62].

Nutlin-3a loading in PNPs was evaluated by HPLC to be 2.5 ± 0.7 wt%. The release of nutlin-3a from the nanoparticles was studied at the same temporal and US stimulation protocol used to treat the cells and in different buffers: at pH 4.5 and 7.4, with or without US stimulation. From Fig. 4a-b, it is evident that the highest cumulative release of the drug is obtained at pH 4.5 plus the ultrasound stimulation (12.5 ± 0.3% of release after 48 h). A more efficient release of nutlin-3a in acidic conditions has been already observed in a previous study, and it is probably due to a higher solubility of the drug in these conditions [39].

Moreover, the stability studies showed that PNPs are less stable at pH 4.5, favoring thus the release of encapsulated substances. At both pH 7.4 and 4.5, US slightly increases the release of nutlin-3a, most likely due to mechanical stress and/or to polarization–depolarization effects in the piezoelectric polymeric core [24].

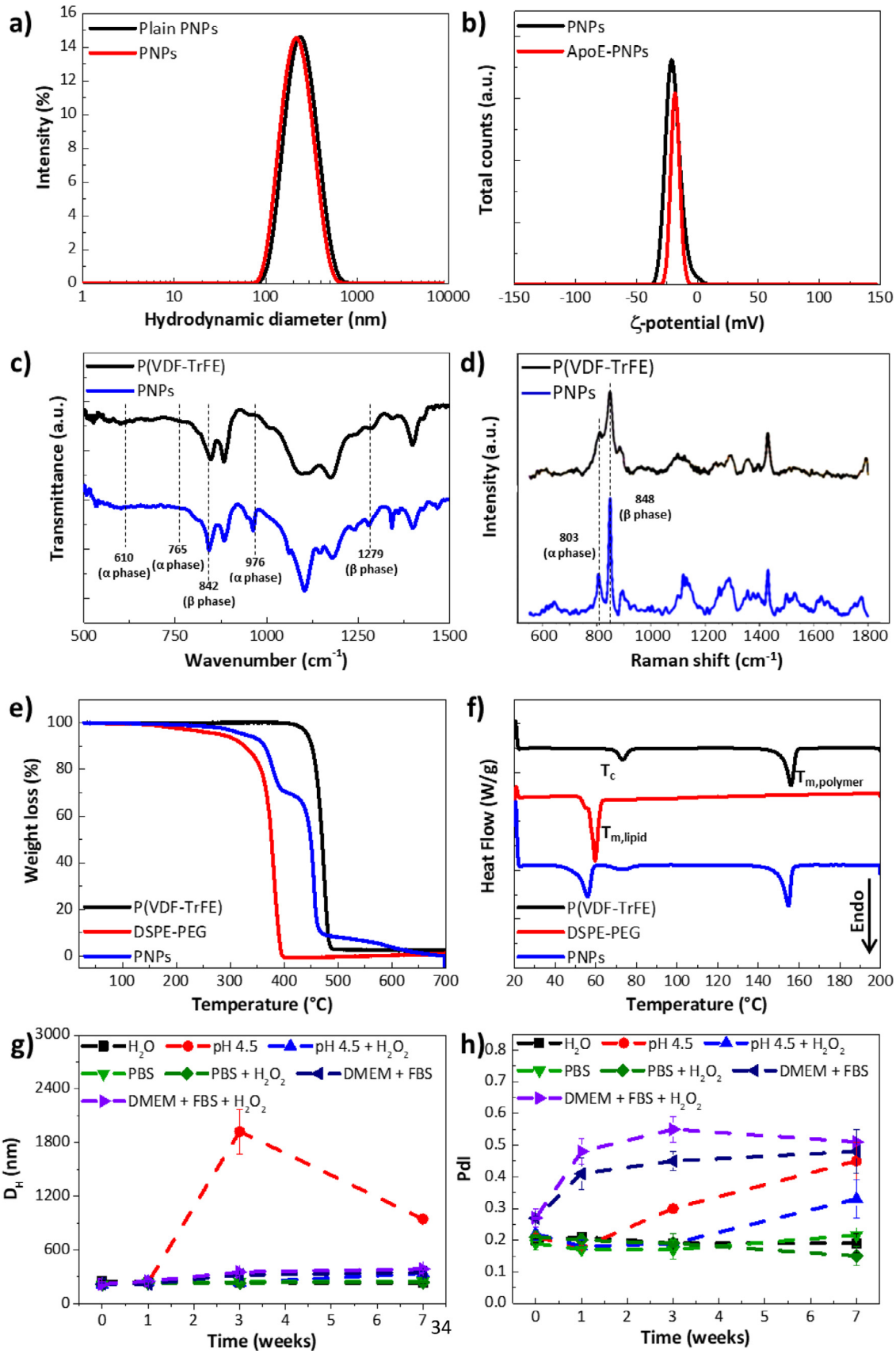

Fig. 2. a) Intensity distribution (%) as a function of the hydrodynamic diameter (nm) and b) ζ-potential (mV) distribution for plain PNPs (black) and functionalized PNPs (red); c) FTIR spectra of P(VDF-TrFE) (black) and PNPs (blue); d) Raman spectra of P(VDF-TrFE) (black) and PNPs (blue); e) TGA thermograms of P(VDF-TrFE) (black), DSPE-PEG (red), and PNPs (blue); f) DSC thermograms of P(VDF-TrFE) (black), DSPE-PEG (red), and PNPs (blue); g) hydrodynamic diameter, D_H, and h) polydispersity index, PdI, of PNPs in different conditions: water (black squares), pH 4.5 (red circles), pH 4.5 + H_2O_2 (blue triangles), PBS (green triangles), PBS + H_2O_2 (green diamonds), DMEM + FBS (dark blue triangles), and DMEM + FBS + H_2O_2 (violet triangles).

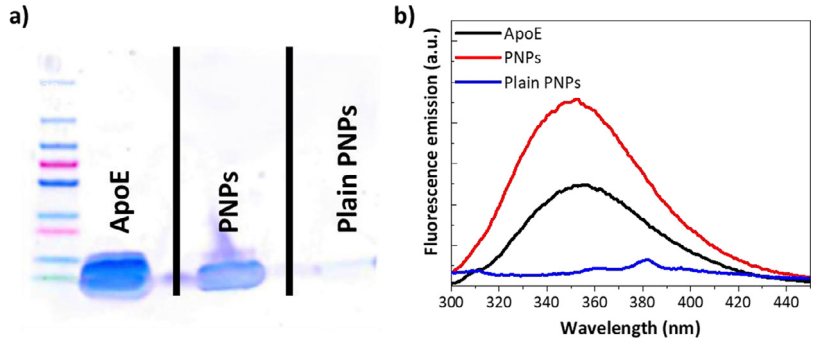

Fig. 3. a) SDS-PAGE of ApoE, functionalized PNPs, and plain PNPs; b) fluorescence spectroscopy of ApoE (black), functionalized PNPs (red), and plain PNPs (blue).

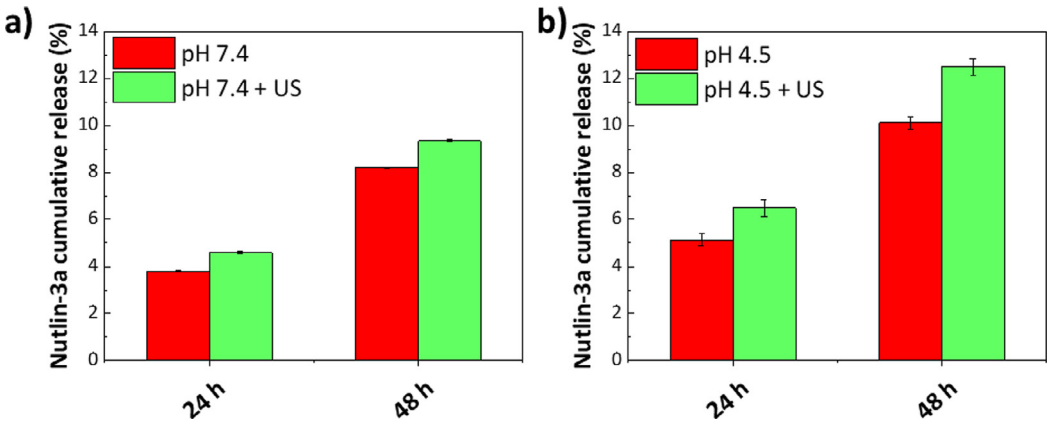

Fig. 4. Nutlin-3a cumulative release (%) from Nut-PNPs at a) pH 7.4 and b) pH 4.5, without (red) and with (green) US stimulus.

These results suggest that PNPs could be more prone to releasing their cargo in cancer cells, that are known to possess a more acidic internal pH as compared to healthy cells, or in acidic intracellular organelles, such as lysosomes, and, more interestingly, that the release can be favored by applying an US stimulus.

Despite this rather low drug release from the nanoparticles, we have to consider thet release studies provide a general overview of the release behavior of the drug, without taking into account the complex interactions and degradation processes that occur within cells (*e.g.*, enzymes might foster the degradation of nanoparticles with consequent release of the drug in the intracellular environment).

To study the ability of plain and functionalized PNPs to cross the BBB, an *ad hoc* fluidic system has been used to recreate the flow conditions that brain capillaries usually experience *in vivo* (Fig. S1) [39,40]. The BBB model was obtained by co-culturing human endothelial cells (hCMEC/D3) and human brain-derived astrocytes (HA) on a porous membrane (as described in the "Materials and Methods" section). It has been previously shown that the presence of both the flow and the astrocytes confers to the endothelial cell cultures the typical BBB phenotype (the formation of tight junction and the expression of specific proteins, for instance) [63,64].

The BBB model showed a TEER of 267 ± 33 $\Omega \cdot cm^2$, and its P_{app} and P_e to rhodamine B-dextran (70 kDa) were around $1.1 \cdot 10^{-6} \pm 0.2 \cdot 10^{-6}$ cm/s and $1.3 \cdot 10^{-6} \pm 0.4 \cdot 10^{-6}$ cm/s, respectively, in agreement with other similar BBB models (Fig. S6) [65,66]. Fig. 5a-b show confocal images of the BBB after interaction with either plain or functionalized PNPs. In both cases, a tight monolayer of hCMEC/D3 cells can be observed. Just a few amounts of nanoparticles are present on the BBB, and in particular, in peripheral position with respect to both hCMEC/D3 and HA. This suggests that, after interacting with the cells of the BBB, nanoparticles are not retained, but rather excreted to the other side *via* transcytosis mechanisms during the perfusion. In particular, it has been previously shown that apolipoprotein E amino acids interact with low-density lipoprotein receptors on the endothelial cells favoring transcytosis, thus avoiding undesired effects caused by lysosomal degradation [33,67]. We, therefore, expect that transcytosis might be the preferred pathway, especially for functionalized PNPs.

Quantitatively, after 48 h from the crossing experiment, the amount of plain PNPs in the lower chamber was 43 ± 1 μg; conversely, the amount of functionalized PNPs was around 55 ± 1 μg, corresponding to an increment of about 20% of nanoparticles that crossed the BBB ($p < 0.05$; *t*-test), confirming the active role of the ApoE peptide in promoting BBB passage.

3.2. Drug and nanoparticle testing in glioblastoma cell lines

The effect of the chemotherapy drug (0.2, 1.0, 5.0, and 25.0 μM) has been tested on different glioblastoma cell lines (T98G, U251, and U87 MG; Fig. S7). T98G cell culture viability was not affected by Nut even when cells were treated with the highest drug concentration (Fig. S7a; $p > 0.05$). In U251 cells, a significant decrease of cell viability was observed for 0.2 μM (15.2% decrease), 1.0 μM (19.6% decrease), 5.0 μM (27.6% decrease), and 25.0 μM (47.7% decrease) Nut concentrations, showing a concentration-dependent sensitivity of these cells to the chemotherapy treatment (Fig. S7b; $p < 0.05$). U87 MG cell viability was also significantly affected at 1.0 μM (40.0% decrease), 5.0 μM (62.9% decrease), and 25.0 μM

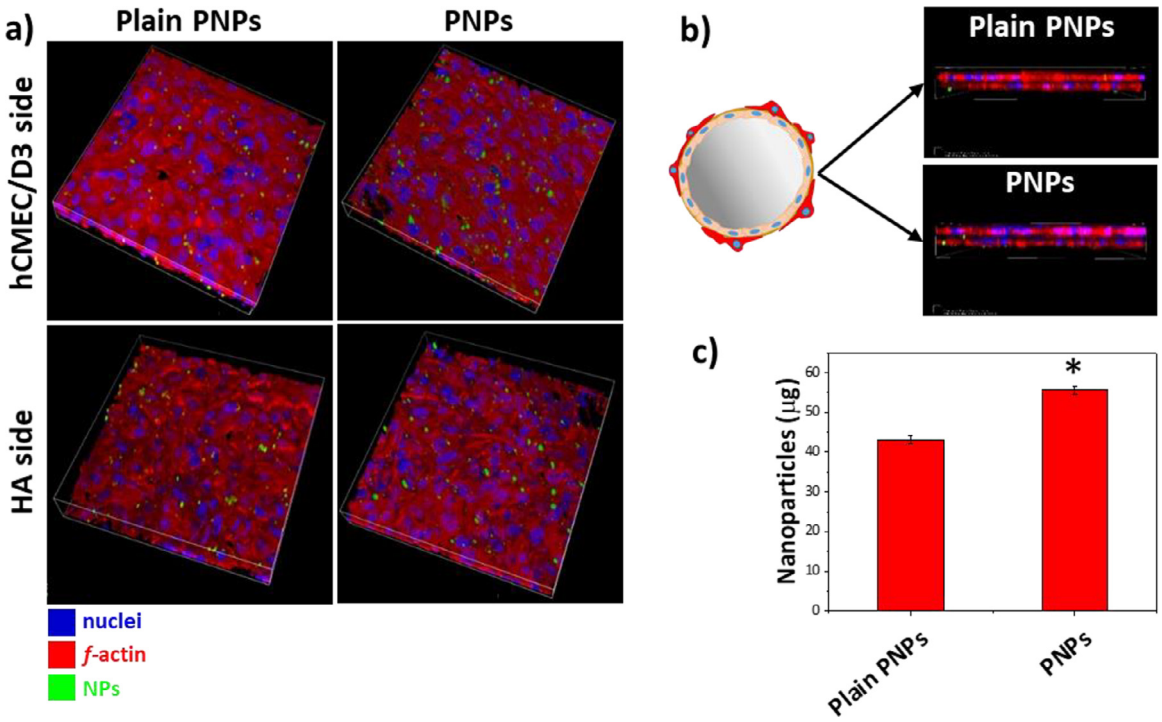

Fig. 5. a) Confocal fluorescence imaging of a typical barrier formed by hCMEC/D3 and HA, with the corresponding uptake of Vybrant™ DiO-labeled plain or functionalized PNPs (in green). Scan area size is $x = 360$ µm, $y = 360$ µm, and $z = 29$ µm; b) Schematic sketch and confocal imaging of a side view of the BBB model. c) Amount of BBB crossed nanoparticles (in μg) at 48 h ($^{*}p < 0.05$).

Nut (75.4% decrease; Fig. S7c; $p < 0.05$). These results showed as T98G cultures were resistant to drug treatment even when treating cells with 25 µM Nut, a concentration 5 times higher with respect to that one found to be toxic towards the other glioblastoma cell lines. The resistance of T98G cells to Nut treatment in this concentration range is in line with observations previously reported in the literature [68].

The toxicity of PNPs and of Nut-loaded PNPs (Nut-PNPs) was assessed by WST-1 assay (Fig. 6). Concerning PNPs (Fig. 6a), no significant effect on cell culture metabolism was observed in cultures treated with 100, 250, 500, or 1000 µg/mL PNPs in the 3 glioblastoma cell lines, demonstrating optimal biocompatibility of the nanomaterial (Fig. 6a; $p > 0.05$). Instead, Nut-PNPs significantly affected the viability of U251, T98G and U87 MG cells (Fig. 6b). Specifically, U251 cells treated with 250, 500, or 1000 µg/mL Nut-PNPs showed significantly decreased viability (76.9 ± 2.8% for 250 µg/mL, 79.1 ± 2.8% for 500 µg/mL, and 80.5 ± 2.8% for 1000 µg/mL Nut-PNPs) with respect to controls (100.0 ± 3.8%; $p < 0.05$). Concerning T98G cells, a significant decrease of viability was found for both 500 µg/mL (81.9 ± 3.4%) and 1000 µg/mL Nut-PNPs (63.4 ± 2.5%) with respect to controls (100.0 ± 2.9%; $p < 0.05$). A significant decrease of the U87 MG culture viability was observed in response to the treatments with 500 (57.7 ± 7.7%), and 1000 (32.0 ± 3.0%) µg/mL Nut-PNPs with respect to controls (100.0 ± 2.1%; $p < 0.05$). Considering that Nut represents 2.5 wt% of Nut-PNPs, Nut concentrations corresponding to 100, 250, 500, and 1000 µg/mL Nut-PNPs were respectively 4.3, 10.8, 21.5, and 43.0 µM. Interestingly, despite T98G cultures were not sensitive to 25 µM Nut, Nut sensitivity was instead observed in these cells when treated with 500 µg/mL Nut-PNPs, corresponding to 21.5 µM Nut. The sensitivity of all the investigated glioblastoma cell lines to Nut-PNPs was considered of great interest for the treatment of GBM cells with different molecular genotypes. The following experiments have been designed to investigate nanoparticle internalization, drug effects and piezoelectric stimulation in the Nut resistant T98G cells by using 500 µg/mL of nanoparticles.

3.3. Cell/nanoparticle interaction

Cellular localization of PNPs in T98G cells was qualitatively assessed at 24 and 72 h of incubation. Fig. 7 shows confocal fluorescence microscopy imaging of nuclei (blue), fluorescently-labeled PNPs (green), and *f*-actin (red). The *f*-actin staining has been used in Fig. 7 as a non-specific cell marker to evaluate the nanoparticle internalization. In these images, the cortical *f*-actin also allows the identification of the edges of single cells. In Fig. 7a and 7b, a single *z*-stack and the 3D confocal reconstruction of the cells during nanoparticle internalization are shown, respectively. The particles were observed in the perinuclear area, and an increase of PNPs signal was detected at 72 h of particle incubation with respect to 24 h of incubation. The progressive and slow internalization rate of the nanoparticles and can be attributed to the negative ζ-potential of the nanoparticles, that is indeed associated with a decreased cytotoxicity [69].

Confocal Raman microscopy imaging was exploited to analyze the internalization of label-free PNPs in T98G cells (Fig. 8). Fig. 8a shows the signals originating from PNPs (in red the β-phase of the PNPs: β-phase: 820 cm^{-1} > Raman shift > 880 cm^{-1}), from cell proteins (in green the amide I region: 1600 cm^{-1} > Raman shift > 1700 cm^{-}1), the bright field (Bf), and the merged images (Merge). Arrows indicate the cell regions with nanoparticles (overlap of the red and green signals in yellow). In Fig. 8b, representative Raman spectra of PNPs outside the cells (PNPs), of cell regions without nanoparticles (Cell), and of cell regions with PNPs (PNPs in cell) are reported. To investigate the possible presence of nanoparticles in cell nuclei, high-resolution confocal Raman microscopy imaging of PNPs (in red the β-phase of the PNPs: β-phase: 820 cm^{-1} > Raman shift > 880 cm^{-1}) and of nuclei (DNA in blue: 760 cm^{-1} > Raman shift > 790 cm^{-1}) was performed (Fig. 8c). The signal of

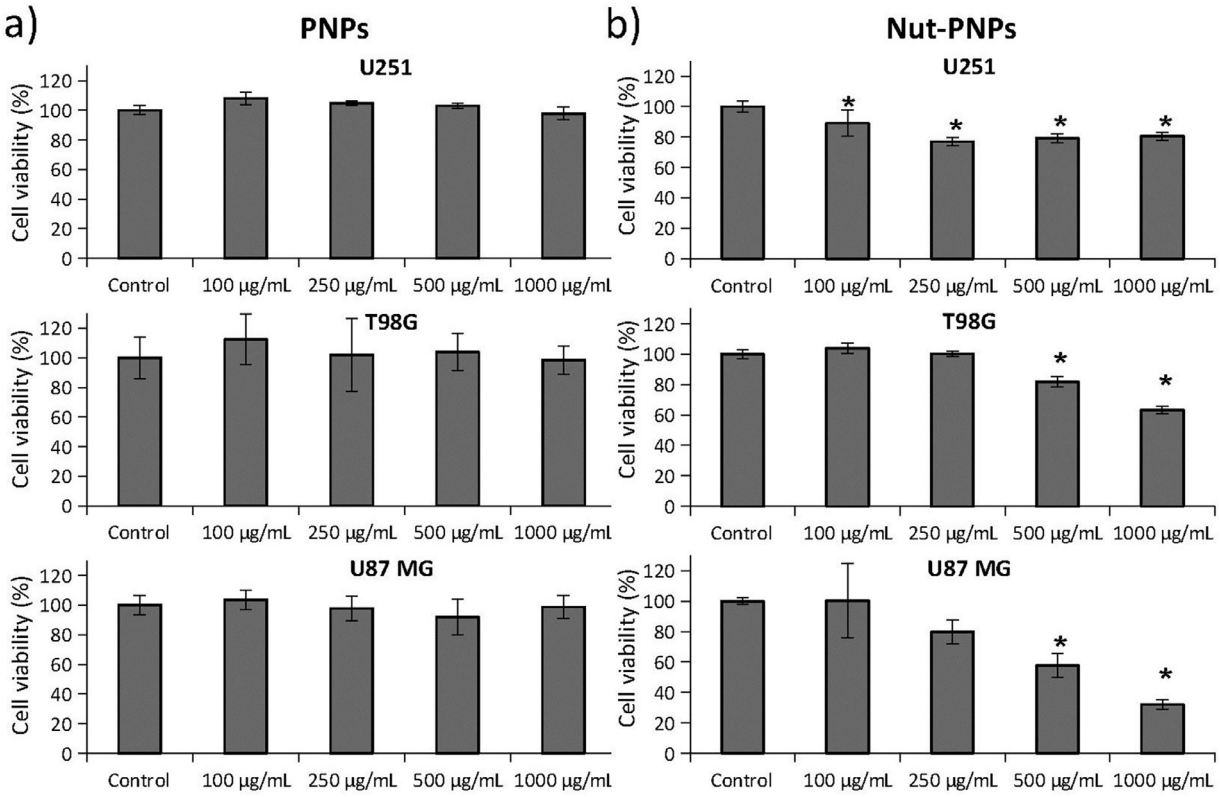

Fig. 6. Investigation of the toxicity of a) PNPs and b) Nut-loaded PNPs (Nut-PNPs) in U251, T98G, and U87 MG cell lines by using WST-1 cell viability assay. $^{*}p < 0.05$.

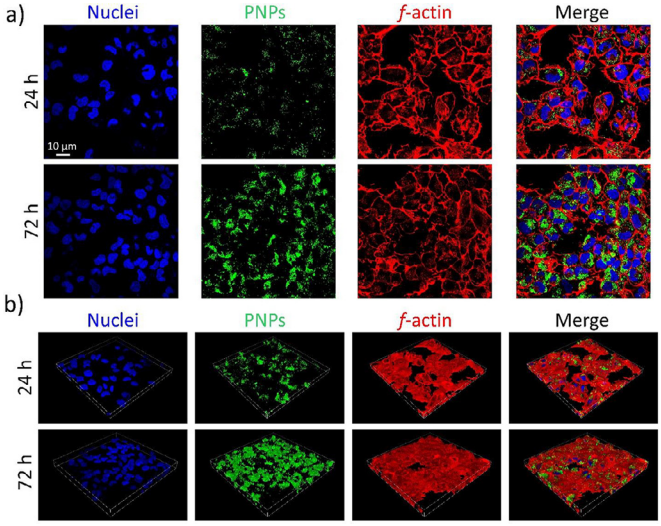

Fig. 7. Internalization of fluorescently-labeled PNPs in T98G cells at 24 and 72 h of incubation. Confocal fluorescence microscopy imaging of nuclei (blue), DiO-stained PNPs (green) and *f*-actin (red). a) Representative single *z*-stack image and b) 3D confocal reconstruction of the cells during nanoparticle internalization.

the PNPs is perinuclear and the imaging shows no co-localization with the signal of the nuclei; representative Raman spectra of the nucleus and of the PNPs on the nucleus are shown in Fig. 8d.. Altogether, these observations confirm label-free PNP uptake by T98G cells with undetectable internalization in cell nuclei.

3.4. Piezoelectric cancer cell stimulation, apoptosis and necrosis

Low-intensity electromagnetic fields are known to induce intracellular Ca^{2+} increments and to reduce cell proliferation [70]; analogous phenomena have been also observed in breast and GBM cells in response to chronic piezoelectric stimulations by exploiting inorganic $BaTiO_3$ NPs activated by US [15,20]. In this work, we investigated for the first time the ability of US-activated organic piezoelectric PNPs to trigger Ca^{2+} fluxes in glioblastoma cells, and we analyzed the effects of the chronic piezoelectric stimulation on cell necrosis and apoptosis.

In Fig. 9, Ca^{2+} imaging of cultures previously incubated with PNPs and stimulated with US (PNPs + US) is shown. Results have been compared with control cultures non-incubated with PNPs and stimulated with US (US). Time-lapse F/F_0 images of Ca^{2+} signal just before (8 min) and during (33, 60 and 85 min) the US stimulation are reported in Fig. 9a. The F/F_0 traces of US-stimulated cells without (in black) and with (in red) PNP pre-incubation are shown in Fig. 9b (the black line at the top of the graph indicates the period of the chronic US stimulation starting at $t = 500$ s). An increase of the Ca^{2+} signal was found just in PNPs + US cultures, indicating that the adopted stimulation protocol was able to induce cellular activation in terms of Ca^{2+} levels only in the presence of the piezoelectric nanotransducers. The sustained high levels of intracellular Ca^{2+} are associated with the chronic pulsed treatment, which consisted in repeated US stimulations (stimuli activated every 2 s that lasted 200 ms each). Such long-duration Ca^{2+} waves can be also induced in cancer cells by chronic electrical stimulations [70]. To our knowledge, this is the first direct demonstration of cell activation assisted by organic piezoelectric nanoparticles, and these findings are in line with previous results obtained with inorganic piezoelectric nanoparticles activated with the same stimulation protocol [15].

The effects of chronic piezoelectric stimulation combined with the Nut chemotherapy drug in terms of apoptosis and necrosis was investigated in T98G cells by considering 8 experimental groups (Fig. 10): controls without (Control) or with (Control + US) US stimulation, cells incubated with free Nut without (Nut) or with

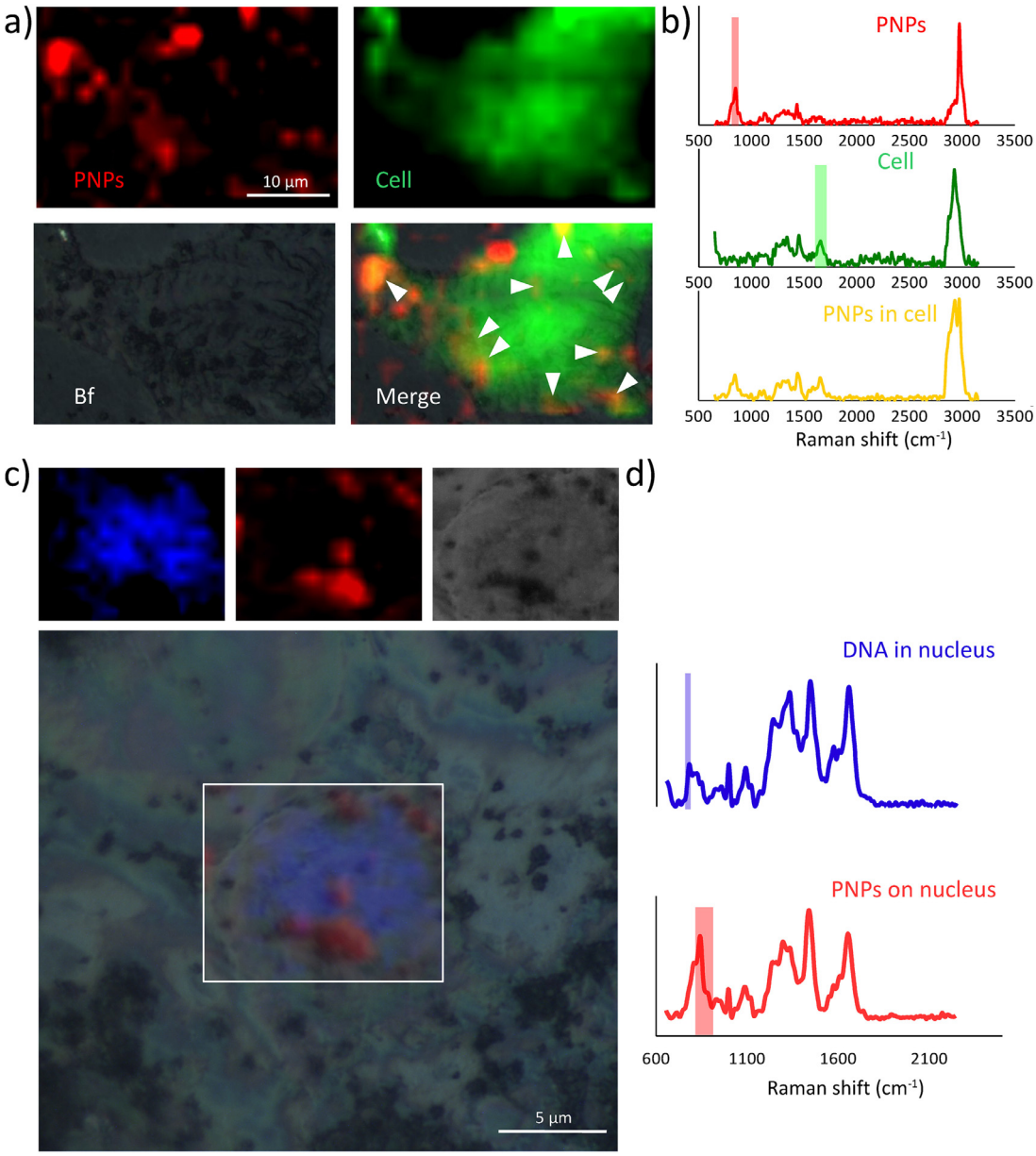

Fig. 8. Confocal Raman microscopy imaging showing label-free PNP interaction with T98G cells at 24 h incubation. a) Raman signal originating from PNPs (in red the β-phase of the PNPs: β-phase: 820 cm^{-1} > Raman shift > 880 cm^{-1}), from cell proteins (in green the amide I region: 1600 cm^{-1} > Raman shift > 1700 cm^{-1}), bright field (Bf), and the merged images (Merge). Arrows indicate the internalized nanoparticles (in yellow the overlap of the red and green signals); b) representative Raman spectra of PNPs outside the cells (PNPs), of cell areas without nanoparticles (Cell), and of cell regions with PNPs (PNPs in cell); c) high-resolution confocal Raman microscopy imaging of PNPs (in red the β-phase of the PNPs: β-phase: 820 cm^{-1} > Raman shift > 880 cm^{-1}) and nuclei (DNA in blue: 760 cm^{-1} > Raman shift > 790 cm^{-1}); d) Raman spectra of the nucleus and of the PNPs on the nucleus.

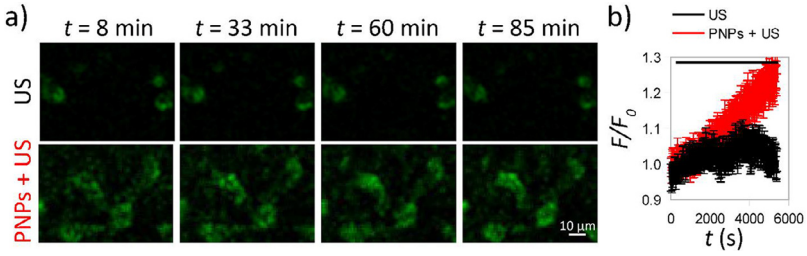

Fig. 9. Ca^{2+} imaging of US-stimulated cells, without or with PNP pre-incubation. a) Representative time-lapse F/F_0 images of Ca^{2+} signal before (8 min) and during (33, 60 and 85 min) US stimulation of T98G cells; b) intracellular F/F_0 traces of US-stimulated cells, without (in black) or with (in red) PNP pre-incubation. The black line at the top of the graph indicates the period of the chronic US stimulation starting at t = 500 s.

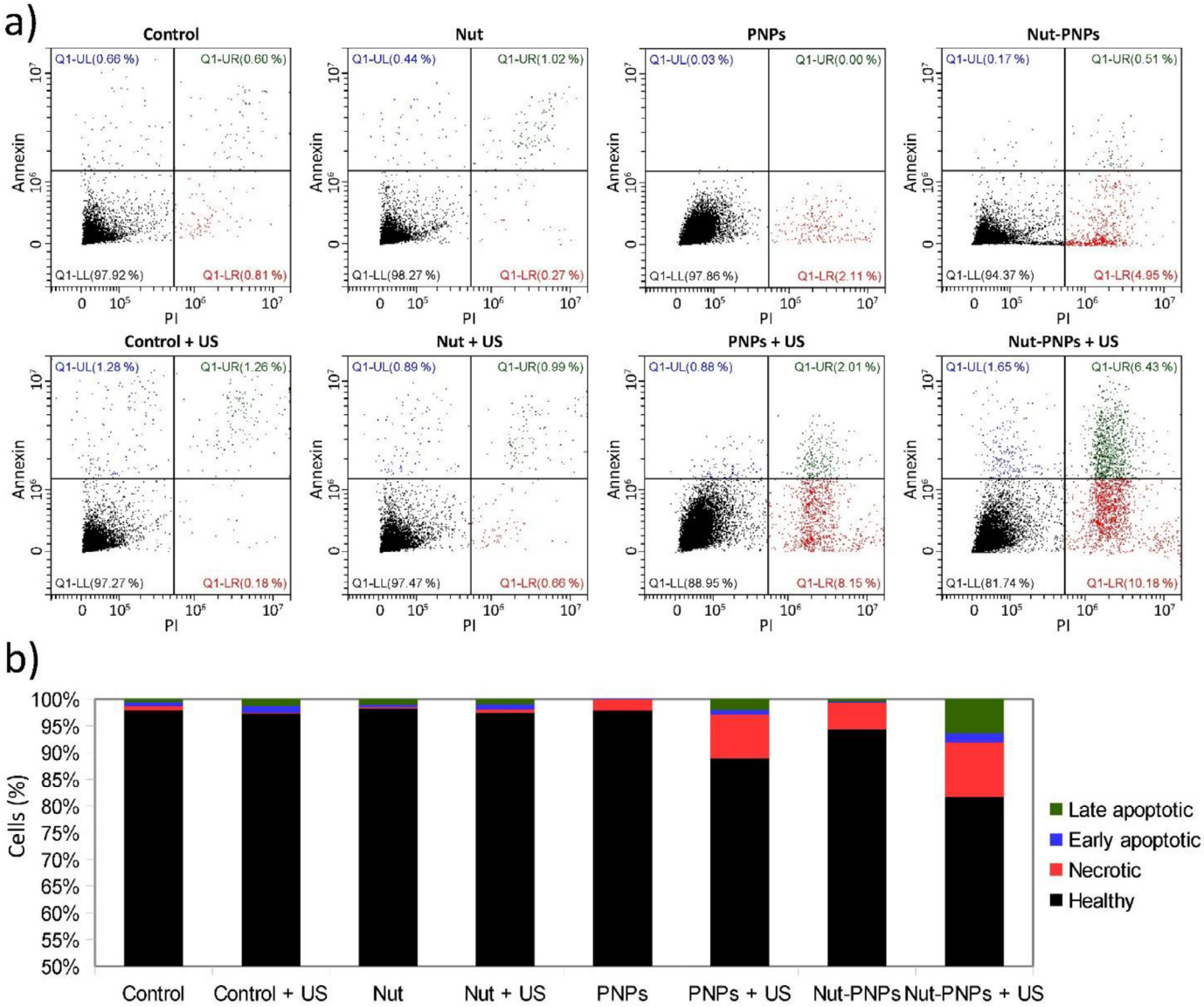

Fig. 10. Apoptosis and necrosis analysis by flow cytometry in T98G cells: controls without (Control) or with (Control + US) US stimulation, cells incubated with free Nut without (Nut) or with (Nut + US) US stimulation, cells incubated with PNPs without (PNPs) or with (PNPs + US) US stimulation, and cells incubated with Nut-PNPs without (Nut-PNPs) or with (Nut-PNPs + US) US stimulation. a) Flow cytometer scatter plots of annexin V *vs.* PI. The populations of necrotic, late apoptotic, early apoptotic, and healthy cells have been highlighted with black, blue, red, and green colors, respectively; b) graph reporting the % of necrotic, late/early apoptotic, and healthy cells.

(Nut + US) US stimulation, cells incubated with PNPs without (PNPs) or with (PNPs + US) US stimulation, and cells incubated with Nut-PNPs without (Nut-PNPs) or with (Nut-PNPs + US) US stimulation. Fig. 10a reports representative flow cytometer scatter plots of annexin V-FITC *vs.* PI for each experimental condition. The populations of necrotic, late apoptotic, early apoptotic, and healthy cells have been highlighted with black, blue, red, and green colors, respectively. The graph reporting the % of the necrotic, late/early apoptotic, and healthy cells in the different experimental classes is shown in Fig. 10b. Control cultures were characterized by 0.8% of necrotic cells, 0.6% of late apoptotic cells, 0.6% of early apoptotic cells, and 98.0% of healthy cells. The most relevant apoptotic/necrotic effects were observed in cultures treated with the combination of piezoelectric stimulation and chemotherapy treatment (Nut-PNPs + US: 10.2% of necrotic, 6.4% of late apoptotic, 1.7% of early apoptotic, and 81.7% of healthy cells). Minor apoptotic/necrotic effects have been observed in stimulated cultures (PNPs + US: 8.2% of necrotic, 2.0% of late apoptotic, 0.9% of early apoptotic, and 88.9% of healthy cells) and in cultures treated with Nut-loaded nanoparticles (Nut-PNPs: 5.0% of necrotic, 0.5% of late apoptotic, 0.2% of early apoptotic, and 94.3% of healthy cells). These findings indicate as the combined piezoelectric and chemotherapy treatment allowed for the best anticancer outcomes in term of apoptosis and necrosis. Moreover, these results suggest as the decreased cell viability observed in cultures treated with Nut-PNPs (Fig. 6b) is associated with toxicity and necrosis. Interestingly, the treatment with 21.5 μM free Nut, which corresponds to the amount of Nut loaded in 500 μg/mL Nut-PNPs, was not able to affect cell viability. The increased toxicity of drug-loaded nanoparticles with respect to the corresponding free drug concentration has been demonstrated in the literature concerning many other cancer models, and can be attributed to the enhanced internalization of the drug in the cells mediated by the nanoparticles [71].

3.5. Cell motility and invasion

Cell migration is the directed movement of cells in response to specific mechanical or chemical signals [72], and it is involved in

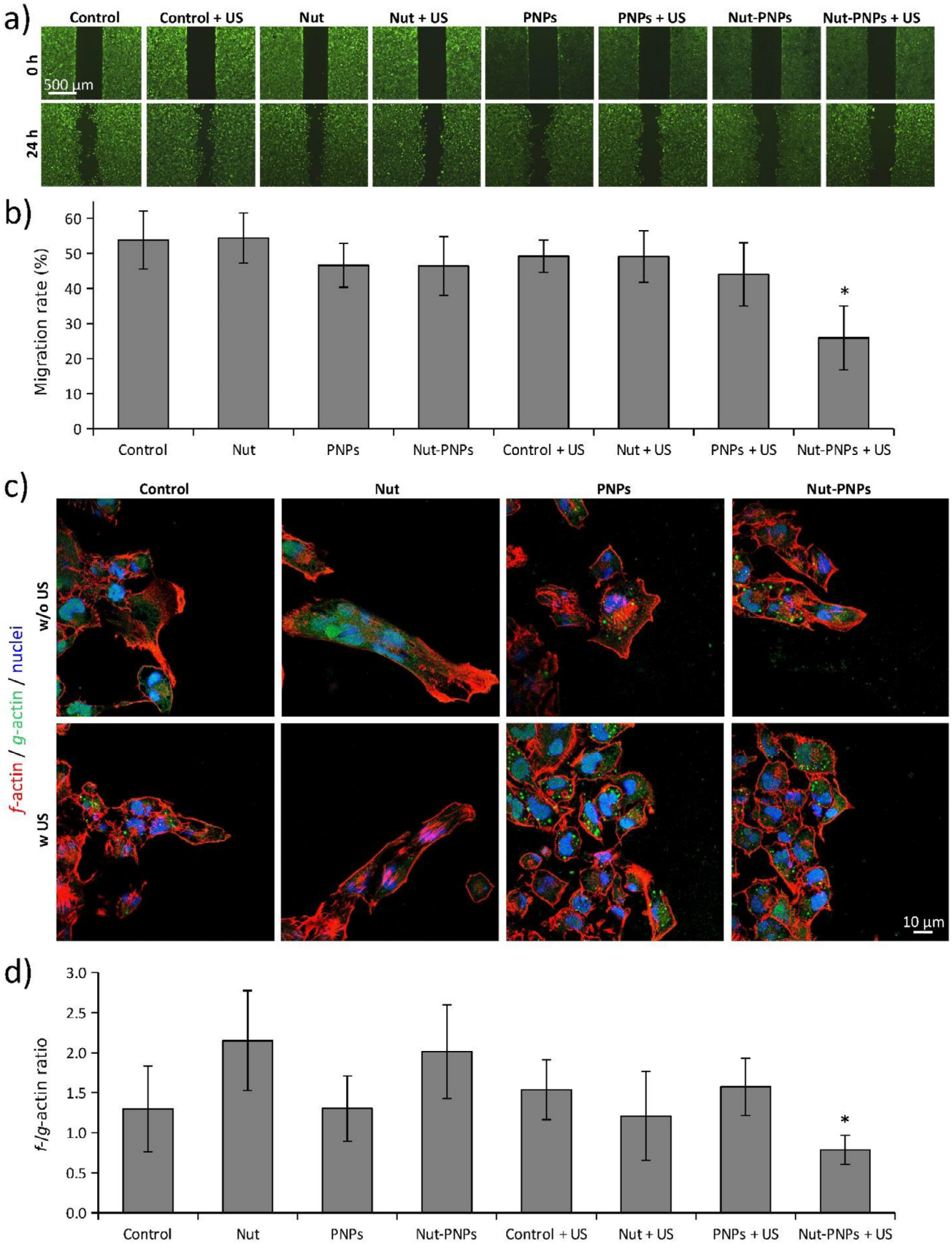

Fig. 11. a) Representative fluorescence images of T98G cells stained with calcein at $t = 0$ h and $t = 24$ h of cell migration; b) percentage of migration rate measured in each experimental class (* $p < 0.05$); c) representative confocal images of T98G cells at the scratch area (fluorescently-labeled PNPs in green, *f*-actin in red, nuclei in blue); d) quantification of *f*-/*g*-actin ratio during cell migration. $^{*}p < 0.05$.

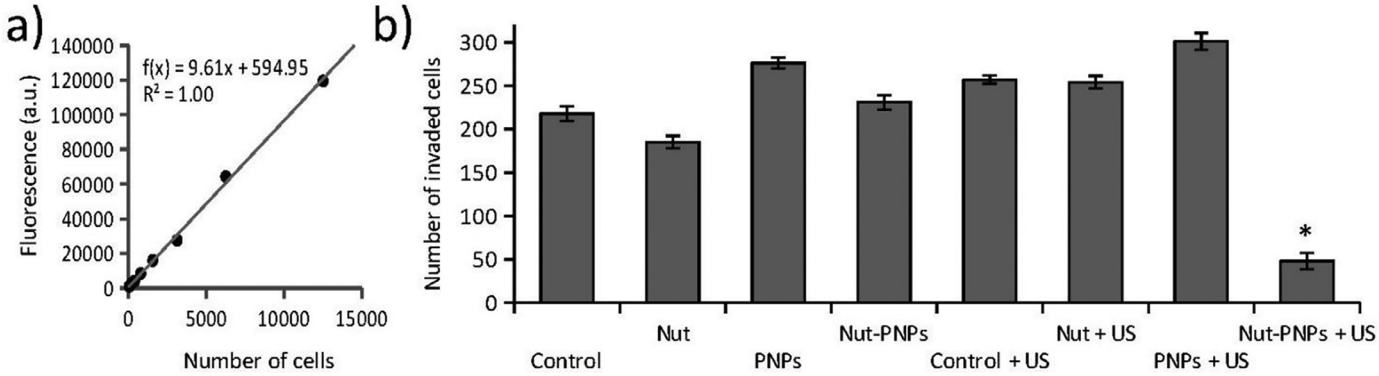

Fig. 12. Invasion of T98G cells through the collagen-coated filter of a transwell system. a) Standard curve reporting fluorescence of T98G stained cells; b) number of T98G cells that underwent invasion through the collagen-coated filter. $^{*}p < 0.05$.

several biological processes including cancer progression, invasiveness and aggressiveness [73]. In this work, *in vitro* cell migration ability of T98G cells was analyzed to assess their migration ability following piezoelectric stimulation and Nut treatment (Fig. 11). Representative images of the scratch area at $t = 0$ h and $t = 24$ h after starting the experiment, and the percentage of migration rate of the 8 experimental classes are reported in Fig. 11a and in Fig. 11b, respectively. The cells treated with Nut-PNPs in the presence of US stimulation (Nut-PNPs + US) showed a reduced migration with respect to the other experimental conditions ($p < 0.05$). Although the bare Nut or PNPs did not affect the migration rate, the combined Nut-PNPs + US treatment significantly decreased the migration rate (25.8 ± 9.1%) with respect to control cultures (Control; migration rate = 53.8 ± 8.2 %; $p < 0.05$).

The actin cytoskeleton has a critical role in organizing cell migration [74]; a characteristic feature of this process is related to the dynamic transition of actin between its monomeric globular *g*-actin and the filamentous *f*-actin form [75]. Fig. 11c shows the confocal fluorescence imaging of T98G cells (*f*-actin in red, *g*-actin in green, nuclei in blue) after treatment. Excluding Nut-PNPs + US experimental treatment, *f*-actin accumulates in the leading edges of the migrated cells and forms lamellipodia. Front-end protrusion and lamellipodia formation play an important role during cell migration, and are an indication of cell motility [76]. Cells treated with Nut-PNPs + US did not show marked protrusions. Moreover, the ratio between *f*-actin and *g*-actin significantly decreased in these cells (Nut-PNPs + US; 0.78 ± 0.18) with respect to control cultures (Controls; 1.30 ± 0.53; $p < 0.05$; Fig. 11d). Since the *f*-actin and *g*-actin respectively represent the polymerized and free monomeric form of actin, the decreased *f*-actin/*g*-actin ratio indicates a reduced level of actin polymerization, which is a phenomenon required during migration [77,78]. The observed cytoskeletal rearrangement is therefore accompanied to a reduced migration level, similarly to analogous situations reported in the literature [79].

Nut is known to reduce cancer cell migration and invasion [80,81], and therefore it may be considered surprising that the treatment with the free drug was not able to reduce motility in our experimental conditions. However, the inhibitory effects of Nut on cell motility, which are known to be mediated by cytoskeletal rearrangements, are limited to p53 wild-type cells [79]. As an example, migration and invasion capabilities of p53-null SAOS osteosarcoma cells are not reduced by 8 μM Nut, a concentration able to affect motility in the p53 wild-type H2OS and HT1080 cancer cells. Considering that T98G cells are p53-mutant cells, a decreased effect of Nut is expected in this line [68]. Likely, piezoelectric stimulation enhanced Nut sensitivity in T98G cells. This observation is in line with the literature, where enhanced chemotherapeutic efficacy and reduced drug resistance were observed in different cancer cells [15,21]. GBM is described as one of the most aggressive and invasive types of malignant brain tumors in adults [82]; the high mortality rate is mainly due to the extensive invasion of cells to adjacent healthy brain tissue and to the migration along blood vessels that results in a recurrence of disease following the treatment [83]. Cancer cell invasion, *i.e.*, the capability of cells to migrate from one area to another through the extracellular matrix (ECM), includes multiple steps such as the adhesion to the ECM molecules, the degradation of the basement membrane matrix and, finally, the migration through the degraded tissue. Here, the invasion capability of T98G cells through a collagen-coated transwell membrane was investigated. As shown in Fig. 12, the number of cells undergoing invasion that crossed the collagen matrix in the Nut-PNPs + US treatment (48 ± 9 cells) was strongly reduced with respect to Control (218 ± 8 cells), as well as with respect to the other experimental conditions (185 ± 7 cells for Nut; 276 ± 6 cells for PNPs; 231 for ± 8 cells for Nut-PNPs; 257 ± 5 cells for Control + US; 254 ± 7 cells for Nut + US; 301 ±.10 cells for PNPs + US). The capability of the anticancer treatment to inhibit cell invasion and to induce cell death is considered fundamental for the success of the therapy [84], and our results indicate the effective inhibition of T98G cell invasion in response to the Nut-PNPs + US treatment, in line with the results obtained in the scratch assay (Fig. 11).

3.6. Proteomic analysis

Proteomic analyses were performed for all the 8 experimental classes (Control, Nut, PNPs, Nut-PNPs, Control + US, Nut+ US, PNPs+ US, Nut-PNPs+ US; Fig. 13). The principal component analysis (PCA) of the first 2 components (accounting respectively for 15.0% and 14.1% of the variance) for each of the 3 performed experiments is reported in Fig. 13a. Basing on PCA, the experimental treatments characterized by the most relevant phenotypic variations with respect to the controls were Nut-PNPs + US, PNPs + US, and Nut-PNPs, experimental classes that also showed significant anticancer effects on T98G cultures (Fig. 10).

Gene ontology (GO) analysis has been carried out to investigate the pathways involved in the observed phenotypic variations. Fig. 13b reports the volcano plot and the GO keywords (downregulated and upregulated pathways are shown in red and green, respectively) regarding the "Nut-PNPs + US *vs.* Control", "PNPs + US *vs.* Control", and Nut-PNPs *vs.* Control" comparisons. In accordance with the PCA analysis, the "Nut-PNPs + US *vs.* Control" comparison is characterized by the major amount of differently represented proteins (DRPs = 814), followed by "Nut-PNPs *vs.* Control" (DRPs = 768), and by "PNPs + US *vs.* Control" (DRPs = 367). Significant GO terms involved in Nut-PNP treatment are "inhibition

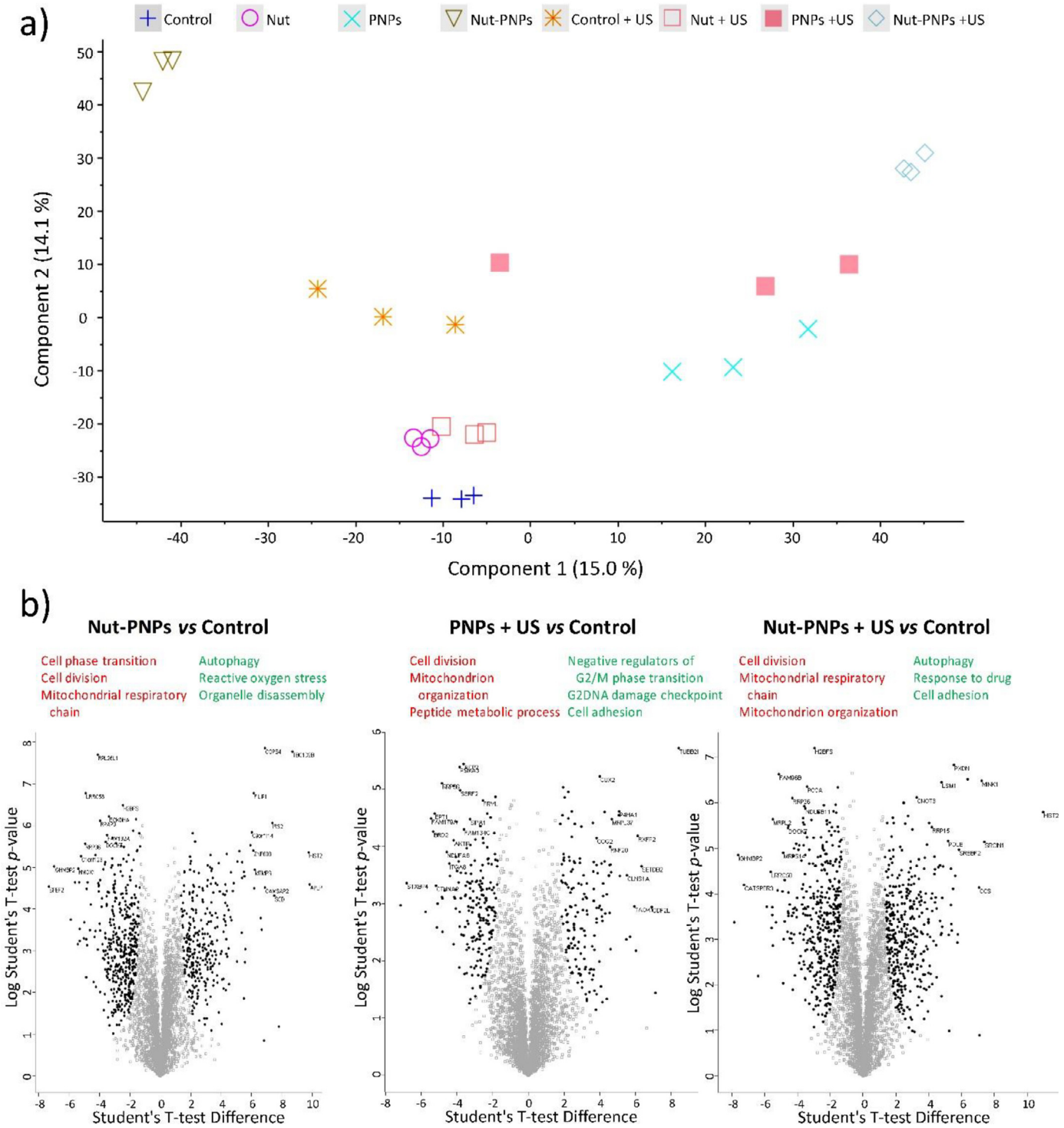

Fig. 13. Proteomic analysis in T98G cells. a) Principal component analysis (PCA) for 3 experiments in each experimental condition; b) volcano plot and GO keywords (downregulated and upregulated pathways are shown in red and green, respectively) regarding the "Nut-PNPs + US *vs.* Control", "PNPs + US *vs.* Control", and "Nut-PNPs *vs.* Control" comparisons.

of cell phase transition", "decreased cell division", "inhibition of the mitochondrial respiratory chain", "autophagy", "reactive oxygen stress", and "organelle disassembly". These GO terms indicate the inhibition of cell proliferation and a stress condition induced by the presence of the Nut-loaded particles. It is also worth noticing that one of the upregulated pathways in cells treated with Nut-PNPs + US is that related to cell responsiveness to drugs (Fig. 13.b). This higher sensitivity to drugs might justify the higher anti-tumor efficacy of Nut-PNPs + US with respect to the non-stimulated counterpart. In these conditions, in fact, we can assume that even a low increase in drug concentration in the intracellular compartment, as evidenced by nutlin-3a release from Nut-PNPs upon US exposure (Fig. 4) can favor toxicity in a more efficient way, as compared to control group without US. Therefore, a higher sensitivity of the cells and a slightly higher concentration of nutlin-3a can cooperate in boosting the anti-tumor activity of Nut-PNPs when

US is applied. Concerning the effects of piezoelectric stimulation, "PNPs + US *vs.* Control", GO terms report an "inhibition of cell division", accompanied by a "reduced peptide metabolic process", "inhibition of mitochondrial organization", and negative regulation of "G/M phase transition". These GO terms indicate a decreased cell metabolism and an inhibition of cell division. Furthermore, in "PNPs + US *vs.* Control" and in "Nut-PNPs + US *vs.* Control" comparisons, the promotion of "cell adhesion" pathways has been observed. This phenomenon is particularly important to counteract the epithelial-mesenchymal transition (EMT) [85]. The acquisition of the mesenchymal phenotype by glioblastoma cells after EMT is associated with increased cell motility and drug resistance, and is involved in glioblastoma progression [86]. The complete list of the GO terms has been reported as Supplementary Information as Table S1-S6.

The reduced cell migration rate observed in Nut-PNPs + US and in PNPs + US stimulated cultures with respect to controls may be associated with the upregulation of the "cell adhesion" pathways; however, it is important to highlight as just in Nut-PNPs + US cultures the reduction in migration rate was statistically significant. In this regard, Nut may play a supporting role in reducing motility in response to piezoelectric stimulation [79,80].

4. Conclusions

In this work, we successfully synthesized piezoelectric hybrid lipid-polymeric nanoparticles, efficiently encapsulating a non-genotoxic drug (nutlin-3a), and functionalized with a peptide (ApoE), that enhances their passage through the BBB. Upon US exposure, PNPs were able to induce a cellular response in terms of Ca^{2+} channel activation, proving the production of an effective electrical cue. Nutlin-loaded PNPs exerted only a mild cytotoxic effect on T98G glioblastoma cells; however, the induction of a US stimulus significantly improved their therapeutic efficacy. In particular, Nut-PNPs upon US exposure were able to reduce cell migration, actin polymerization, and invasion ability of T98G cells, while fostering apoptotic and necrotic events; from proteomic analysis, significant GO terms involved in this combined treatment resulted to be the "inhibition of cell division", "promotion of autophagy", and "promotion of cell adhesion" pathways. Taken all together, these results clearly show the potentialities of biocompatible organic piezoelectric nanomaterials and ultrasound stimulation in the treatment of extremely aggressive and invasive cancers such as glioblastoma. Moreover, wireless activation of the anticancer action paves the way to a less invasive, more focused and efficient approach that could potentially target also deep-seated tumors, without recurring to surgical intervention or invasive therapeutic protocols.

Disclosure

The authors declare that they have no known competing financial interests or personal relationships that could have appeared to influence the work reported in this paper.

Declaration of Competing Interest

The authors declare that they have no known competing financial interests or personal relationships that could have appeared to influence the work reported in this paper.

Acknowledgements

This work has received funding from the European Research Council (ERC) under the European Union's Horizon 2020 research and innovation program (grant agreement N°709613, SLaMM). The authors would also like to acknowledge Mr. Carlo Filippeschi (*Istituto Italiano di Tecnologia*, Italy) and Dr. Giammarino Pugliese (*Istituto Italiano di Tecnologia*, Italy) for their support in SEM analysis and in TGA measurements, respectively.

Supplementary materials

Supplementary material associated with this article can be found, in the online version, at doi:10.1016/j.actbio.2021.04.005.

References

[1] A. Degl'Innocenti, N. di Leo, G. Ciofani, Genetic Hallmarks and Heterogeneity of Glioblastoma in the Single-Cell Omics Era, Adv. Ther. 3 (2020) 1900152, doi:10.1002/adtp.201900152.
[2] E.C. Holland, Glioblastoma multiforme: The terminator, Proc. Natl. Acad. Sci. U. S. A. 97 (2000) 6242–6244, doi:10.1073/pnas.97.12.6242.
[3] J.R.D. Pearson, T. Regad, Targeting cellular pathways in glioblastoma multiforme, Signal Transduct. Target. Ther. 2 (2017) 1–11, doi:10.1038/sigtrans.2017.40.
[4] R. Jelsma, P.C. Bucy, The treatment of glioblastoma multiforme of the brain, J. Neurosurg. 27 (1967) 388–400, doi:10.3171/jns.1967.27.5.0388.
[5] N. Ishii, M. Tada, M.F. Hamou, R.C. Janzer, K. Meagher-Villemure, O.D. Wiestler, N. De Tribolet, E.G. Van Meir, Cells with TP53 mutations in low grade astrocytic tumors evolve clonally to malignancy and are an unfavorable prognostic factor, Oncogene (1999), doi:10.1038/sj.onc.1203241.
[6] W.M. Pardridge, Drug targeting to the brain, Pharm. Res. (2007), doi:10.1007/s11095-007-9324-2.
[7] C.P. Haar, P. Hebbar, G.C. Wallace, A. Das, W.A. Vandergrift, J.A. Smith, P. Giglio, S.J. Patel, S.K. Ray, N.L. Banik, Drug resistance in glioblastoma: a mini review, Neurochem. Res. 37 (2012) 1192–1200, doi:10.1007/s11064-011-0701-1.
[8] C. Martinelli, C. Pucci, G. Ciofani, Nanostructured carriers as innovative tools for cancer diagnosis and therapy, APL Bioeng. 3 (2019), doi:10.1063/1.5079943.
[9] C. Pucci, C. Martinelli, G. Ciofani, Innovative approaches for cancer treatment: Current perspectives and new challenges, Ecancermedicalscience 13 (2019) 1–26, doi:10.3332/ecancer.2019.961.
[10] D. Hymel, B.R. Peterson, Synthetic cell surface receptors for delivery of therapeutics and probes, Adv. Drug Deliv. Rev. (2012), doi:10.1016/j.addr.2012.02.007.
[11] H. Gao, Progress and perspectives on targeting nanoparticles for brain drug delivery, Acta Pharm. Sin. B. 6 (2016) 268–286, doi:10.1016/j.apsb.2016.05.013.
[12] J. Li, H. Duan, K. Pu, Nanotransducers for near-infrared photoregulation in biomedicine, Adv. Mater. 31 (2019), doi:10.1002/adma.201901607.
[13] J. Yang, Z. Shi, R. Liu, Y. Wu, X. Zhang, Combined-therapeutic strategies synergistically potentiate glioblastoma multiforme treatment via nanotechnology, Theranostics 10 (2020) 3223–3239, doi:10.7150/thno.40298.
[14] A. Marino, A. Camponovo, A. Degl'Innocenti, M. Bartolucci, C. Tapeinos, C. Martinelli, D. De Pasquale, F. Santoro, V. Mollo, S. Arai, M. Suzuki, Y. Harada, A. Petretto, G. Ciofani, Multifunctional temozolomide-loaded lipid superparamagnetic nanovectors: dual targeting and disintegration of glioblastoma spheroids by synergic chemotherapy and hyperthermia treatment, Nanoscale 11 (2019) 21227–21248, doi:10.1039/c9nr07976a.
[15] A. Marino, E. Almici, S. Migliorin, C. Tapeinos, M. Battaglini, V. Cappello, M. Marchetti, G. de Vito, R. Cicchi, F.S. Pavone, G. Ciofani, Piezoelectric barium titanate nanostimulators for the treatment of glioblastoma multiforme, J. Colloid Interface Sci. 538 (2019) 449–461, doi:10.1016/j.jcis.2018.12.014.
[16] L. Liu, B. Chen, K. Liu, J. Gao, Y. Ye, Z. Wang, N. Qin, D.A. Wilson, Y. Tu, F. Peng, Wireless manipulation of magnetic/piezoelectric micromotors for precise neural stem-like cell stimulation, Adv. Funct. Mater. 30 (2020) 1910108, doi:10.1002/adfm.201910108.
[17] A. Cafarelli, A. Verbeni, A. Poliziani, P. Dario, A. Menciassi, L. Ricotti, Tuning acoustic and mechanical properties of materials for ultrasound phantoms and smart substrates for cell cultures, Acta Biomater. 49 (2017) 368–378, doi:10.1016/j.actbio.2016.11.049.
[18] B. Ma, F. Liu, Z. Li, J. Duan, Y. Kong, M. Hao, S. Ge, H. Jiang, H. Liu, Piezoelectric nylon-11 nanoparticles with ultrasound assistance for high-efficiency promotion of stem cell osteogenic differentiation, J. Mater. Chem. B. 7 (2019) 1847–1854, doi:10.1039/c8tb03321h.
[19] A. Marino, S. Arai, Y. Hou, E. Sinibaldi, M. Pellegrino, Y.T. Chang, B. Mazzolai, V. Mattoli, M. Suzuki, G. Ciofani, Piezoelectric nanoparticle-assisted wireless neuronal stimulation, ACS Nano 9 (2015) 7678–7689, doi:10.1021/acsnano.5b03162.
[20] A. Marino, M. Battaglini, D. De Pasquale, A. Degl'Innocenti, G. Ciofani, Ultrasound-activated piezoelectric nanoparticles inhibit proliferation of breast cancer cells, Sci. Rep. 8 (2018), doi:10.1038/s41598-018-24697-1.
[21] D. Janigro, C. Perju, V. Fazio, K. Hallene, G. Dini, M.K. Agarwal, L. Cucullo, Alternating current electrical stimulation enhanced chemotherapy: a novel strategy to bypass multidrug resistance in tumor cells, BMC Cancer 6 (2006) 72, doi:10.1186/1471-2407-6-72.
[22] R. Stupp, S. Taillibert, A. Kanner, W. Read, D.M. Steinberg, B. Lhermitte, S. Toms, A. Idbaih, M.S. Ahluwalia, K. Fink, F. Di Meco, F. Lieberman, J.J. Zhu, G. Stragliotto, D.D. Tran, S. Brem, A.F. Hottinger, E.D. Kirson, G. Lavy-Shahaf, U. Weinberg, C.Y. Kim, S.H. Paek, G. Nicholas, J. Burna, H. Hirte, M. Weller,

Y. Palti, M.E. Hegi, Z. Ram, Effect of tumor-treating fields plus maintenance temozolomide vs maintenance temozolomide alone on survival in patients with glioblastoma a randomized clinical trial, JAMA - J. Am. Med. Assoc. 318 (2017) 2306–2316, doi:10.1001/jama.2017.18718.
[23] L. Cucullo, G. Dini, K.L. Hallene, V. Fazio, E.V. Ilkanich, C. Igboechi, K.M. Kight, M.K. Agarwal, M. Garrity-Moses, D. Janigro, Very low intensity alternating current decreases cell proliferation, Glia 51 (2005) 65–72, doi:10.1002/glia.20188.
[24] K. Kapat, Q.T.H. Shubhra, M. Zhou, S. Leeuwenburgh, Piezoelectric nanobiomaterials for biomedicine and tissue regeneration, Adv. Funct. Mater. 30 (2020) 1909045, doi:10.1002/adfm.201909045.
[25] G.G. Genchi, L. Ceseracciu, A. Marino, M. Labardi, S. Marras, F. Pignatelli, L. Bruschini, V. Mattoli, G. Ciofani, P(VDF-TrFE)/BaTiO3 nanoparticle composite films mediate piezoelectric stimulation and promote differentiation of SH-SY5Y neuroblastoma cells, Adv. Healthc. Mater. 5 (2016) 1808–1820, doi:10.1002/adhm.201600245.
[26] P. Hitscherich, S. Wu, R. Gordan, L.H. Xie, T. Arinzeh, E.J. Lee, The effect of PVDF-TrFE scaffolds on stem cell derived cardiovascular cells, Biotechnol. Bioeng. 113 (2016) 1577–1585, doi:10.1002/bit.25918.
[27] G.G. Genchi, E. Sinibaldi, L. Ceseracciu, M. Labardi, A. Marino, S. Marras, G. De Simoni, V. Mattoli, G. Ciofani, Ultrasound-activated piezoelectric P(VDF-TrFE)/boron nitride nanotube composite films promote differentiation of human SaOS-2 osteoblast-like cells, Nanomedicine Nanotechnology, Biol. Med. 14 (2018) 2421–2432, doi:10.1016/j.nano.2017.05.006.
[28] Z. Xiao, Q. Dong, P. Sharma, Y. Yuan, B. Mao, W. Tian, A. Gruverman, J. Huang, Synthesis and application of ferroelectric P(VDF-TrFE) nanoparticles in organic photovoltaic devices for high efficiency, Adv. Energy Mater. 3 (2013) 1581–1588, doi:10.1002/aenm.201300396.
[29] T. Date, V. Nimbalkar, J. Kamat, A. Mittal, R.I. Mahato, D. Chitkara, Lipid-polymer hybrid nanocarriers for delivering cancer therapeutics, J. Control. Release. 271 (2018) 60–73, doi:10.1016/j.jconrel.2017.12.016.
[30] P. Chène, Inhibiting the p53-MDM2 interaction: An important target for cancer therapy, Nat. Rev. Cancer. 3 (2003) 102–109, doi:10.1038/nrc991.
[31] P. Secchiero, F. Corallini, A. Gonelli, R. Dell'Eva, M. Vitale, S. Capitani, A. Albini, G. Zauli, Antiangiogenic activity of the MDM2 antagonist nutlin-3, Circ. Res. 100 (2007) 61–69, doi:10.1161/01.RES.0000253975.76198.ff.
[32] F. Re, I. Cambianica, C. Zona, S. Sesana, M. Gregori, R. Rigolio, B.La Ferla, F. Nicotra, G. Forloni, A. Cagnotto, M. Salmona, M. Masserini, G. Sancini, Functionalization of liposomes with ApoE-derived peptides at different density affects cellular uptake and drug transport across a blood-brain barrier model, Nanomedicine Nanotechnology, Biol. Med. 7 (2011) 551–559, doi:10.1016/j.nano.2011.05.004.
[33] B. Dehouck, L. Fenart, M.P. Dehouck, A. Pierce, G. Torpier, R. Cecchelli, A new function for the LDL receptor: transcytosis of LDL across the blood-brain barrier, J. Cell Biol. 138 (1997) 877–889, doi:10.1083/jcb.138.4.877.
[34] Y. Jiang, J. Zhang, F. Meng, Z. Zhong, Apolipoprotein e peptide-directed chimeric polymersomes mediate an ultrahigh-efficiency targeted protein therapy for glioblastoma, ACS Nano 12 (2018) 11070–11079, doi:10.1021/acsnano.8b05265.
[35] J.A.R. Nicoll, E. Zunarelli, R. Rampling, L.S. Murray, V. Papanastassiou, J. Stewart, Involvement of apolipoprotein E in glioblastoma: Immunohistochemistry and clinical outcome, Neuroreport 14 (2003) 1923–1926, doi:10.1097/00001756-200310270-00008.
[36] V. Sencadas, V.M. Moreira, S. Lanceros-Mendéz, A.S. Pouzada, R. Gregório, α - To - β transformation on PVDF films obtained by uniaxial stretch, Mater. Sci. Forum (2006), doi:10.4028/www.scientific.net/msf.514-516.872.
[37] P. Martins, A.C. Lopes, S. Lanceros-Mendez, Electroactive phases of poly(vinylidene fluoride): determination, processing and applications, Prog. Polym. Sci. 39 (2014) 683–706, doi:10.1016/j.progpolymsci.2013.07.006.
[38] F. Xu, K. Zhang, Y. Zhou, Z. Qu, H. Wang, Y. Zhang, H. Zhou, C. Yan, Facile preparation of highly oriented poly(vinylidene fluoride) uniform films and their ferro- and piezoelectric properties, RSC Adv. 7 (2017) 17038–17043, doi:10.1039/c7ra00586e.
[39] C. Pucci, D. De Pasquale, A. Marino, C. Martinelli, S. Lauciello, G. Ciofani, Hybrid magnetic nanovectors promote selective glioblastoma cell death through a combined effect of lysosomal membrane permeabilization and chemotherapy, ACS Appl. Mater. Interfaces. 12 (2020) 29037–29055, doi:10.1021/acsami.0c05556.
[40] D. De Pasquale, A. Marino, C. Tapeinos, C. Pucci, S. Rocchiccioli, E. Michelucci, F. Finamore, L. McDonnell, A. Scarpellini, S. Lauciello, M. Prato, A. Larrañaga, F. Drago, G. Ciofani, Homotypic targeting and drug delivery in glioblastoma cells through cell membrane-coated boron nitride nanotubes, Mater. Des. 192 (2020), doi:10.1016/j.matdes.2020.108742.
[41] I. Papademetriou, E. Vedula, J. Charest, T. Porter, Effect of flow on targeting and penetration of angiopep-decorated nanoparticles in a microfluidic model blood-brain barrier, PLoS One 13 (2018) 1–18, doi:10.1371/journal.pone.0205158.
[42] A. Siflinger-Birnboim, P.J. del Vecchio, J.A. Cooper, F.A. Blumenstock, J.M. Shepard, A.B. Malik, Molecular sieving characteristics of the cultured endothelial monolayer, J. Cell. Physiol. 132 (1987) 111–117, doi:10.1002/jcp.1041320115.
[43] M. Heymans, E. Sevin, F. Gosselet, S. Lundquist, M. Culot, Mimicking brain tissue binding in an in vitro model of the blood-brain barrier illustrates differences between in vitro and in vivo methods for assessing the rate of brain penetration, Eur. J. Pharm. Biopharm. 127 (2018) 453–461, doi:10.1016/j.ejpb.2018.03.007.
[44] A.D. Wong, M. Ye, A.F. Levy, J.D. Rothstein, D.E. Bergles, P.C. Searson, The blood-brain barrier: an engineering perspective, Front. Neuroeng. 6 (2013) 1–22, doi:10.3389/fneng.2013.00007.
[45] A. Marino, S. Arai, Y. Hou, A. Degl'Innocenti, V. Cappello, B. Mazzolai, Y.T. Chang, V. Mattoli, M. Suzuki, G. Ciofani, Gold nanoshell-mediated remote myotube activation, ACS Nano 11 (2017) 2494–2505, doi:10.1021/acsnano.6b08202.
[46] S. Rivas-Arancibia, E. Rodríguez-Martínez, I. Badillo-Ramírez, U. López-González, J.M. Saniger, Structural changes of amyloid beta in hippocampus of rats exposed to ozone: a Raman spectroscopy study, Front. Mol. Neurosci. 10 (2017), doi:10.3389/fnmol.2017.00137.
[47] K.A. Okotrub, N.V. Surovtsev, V.F. Semeshin, L.V. Omelyanchuk, Raman spectroscopy for DNA quantification in cell nucleus, Cytom. Part A. 87 (2015) 68–73, doi:10.1002/cyto.a.22585.
[48] D.A. Guzmán-Embús, M. Orrego Cardozo, C. Vargas-Hernández, Genomic DNA characterization of pork spleen by Raman spectroscopy, J. Appl. Phys. 114 (2013) 194704, doi:10.1063/1.4831948.
[49] C. Rojas, M. Tedesco, P. Massobrio, A. Marino, G. Ciofani, S. Martinoia, R. Raiteri, Acoustic stimulation can induce a selective neural network response mediated by piezoelectric nanoparticles, J. Neural Eng. 15 (2018), doi:10.1088/1741-2552/aaa140.
[50] C. Tapeinos, A. Marino, M. Battaglini, S. Migliorin, R. Brescia, A. Scarpellini, C. De Julián Fernández, M. Prato, F. Drago, G. Ciofani, Stimuli-responsive lipid-based magnetic nanovectors increase apoptosis in glioblastoma cells through synergic intracellular hyperthermia and chemotherapy, Nanoscale 11 (2019) 72–88, doi:10.1039/c8nr05520c.
[51] N.A. Kulak, G. Pichler, I. Paron, N. Nagaraj, M. Mann, Minimal, encapsulated proteomic-sample processing applied to copy-number estimation in eukaryotic cells, Nat. Methods. 11 (2014) 319–324, doi:10.1038/nmeth.2834.
[52] J. Cox, M. Mann, MaxQuant enables high peptide identification rates, individualized p.p.b.-range mass accuracies and proteome-wide protein quantification, Nat. Biotechnol. 26 (2008) 1367–1372, doi:10.1038/nbt.1511.
[53] S. Tyanova, T. Temu, P. Sinitcyn, A. Carlson, M.Y. Hein, T. Geiger, M. Mann, J. Cox, The Perseus computational platform for comprehensive analysis of (prote)omics data, Nat. Methods. 13 (2016) 731–740, doi:10.1038/nmeth.3901.
[54] C.S. Greene, A. Krishnan, A.K. Wong, E. Ricciotti, R.A. Zelaya, D.S. Himmelstein, R. Zhang, B.M. Hartmann, E. Zaslavsky, S.C. Sealfon, D.I. Chasman, G.A. FitzGerald, K. Dolinski, T. Grosser, O.G. Troyanskaya, Understanding multicellular function and disease with human tissue-specific networks, Nat. Genet. 47 (2015) 569, doi:10.1038/NG.3259.
[55] N. Meng, X. Zhu, R. Mao, M.J. Reece, E. Bilotti, Nanoscale interfacial electroactivity in PVDF /PVDF-TrFE blended films with enhanced dielectric and ferroelectric properties †, J. Mater. Chem. C. 5 (2017) 3296–3305, doi:10.1039/c7tc00162b.
[56] A.J. Lovinger, T. Furukawa, G.T. Davis, M.G. Broadhurst, Crystallographic changes characterizing the Curie transition in three ferroelectric copolymers of vinylidene fluoride and trifluoroethylene: 1. As-crystallized samples, Polymer (Guildf) 24 (1983) 1225–1232, doi:10.1016/0032-3861(83)90050-2.
[57] A.J. Lovinger, Ferroelectric Polymers, Science (80-.) 220 (1983) 1115–1121.
[58] G.T. Davis, J.E. McKinney, M.G. Broadhurst, S.C. Roth, Electric-field-induced phase changes in poly(vinylidene fluoride), J. Appl. Phys. 49 (1978) 4998, doi:10.1063/1.324446.
[59] K. Matsushige, K. Nagata, S. Imada, T. Takemura, The II-I crystal transformation of poly(vinylidene fluoride) under tensile and compressional stresses, Polymer (Guildf) 21 (1980) 1391–1397, doi:10.1016/0032-3861(80)90138-X.
[60] G. Teyssedre, DSC and TSC study of a VDF /TrFE copolymer, Thermochim. Acta. 226 (1993) 65–75.
[61] F. Bahadori, G. Topçu, M.S. Ero, H. Önyüksel, A New Lipid-Based Nano Formulation of Vinorelbine, AAPS PharmSciTech 15 (2014) 1138–1148, doi:10.1208/s12249-014-0146-3.
[62] A.M. Alkilany, L. Zhu, H. Weller, A. Mews, W.J. Parak, M. Barz, N. Feliu, Ligand density on nanoparticles: A parameter with critical impact on nanomedicine, Adv. Drug Deliv. Rev. 143 (2019) 22–36, doi:10.1016/j.addr.2019.05.010.
[63] S. Santaguida, D. Janigro, M. Hossain, E. Oby, E. Rapp, L. Cucullo, Side by side comparison between dynamic versus static models of blood-brain barrier in vitro: A permeability study, Brain Res 1109 (2006) 1–13, doi:10.1016/j.brainres.2006.06.027.
[64] H. Xu, Z. Li, Y. Yu, S. Sizdahkhani, W.S. Ho, F. Yin, L. Wang, G. Zhu, M. Zhang, L. Jiang, Z. Zhuang, J. Qin, A dynamic in vivo-like organotypic blood-brain barrier model to probe metastatic brain tumors, Sci. Rep. 6 (2016) 36670, doi:10.1038/srep36670.
[65] B.B. Weksler, E.A. Subileau, N. Perrière, P. Charneau, K. Holloway, M. Leveque, H. Tricoire-Leignel, A. Nicotra, S. Bourdoulous, P. Turowski, D.K. Male, F. Roux, J. Greenwood, I.A. Romero, P.O. Couraud, Blood-brain barrier-specific properties of a human adult brain endothelial cell line, FASEB J 19 (2005) 1872–1874, doi:10.1096/fj.04-3458fje.
[66] H.C. Helms, N.J. Abbott, M. Burek, R. Cecchelli, P.O. Couraud, M.A. Deli, C. Förster, H.J. Galla, I.A. Romero, E.V. Shusta, M.J. Stebbins, E. Vandenhaute, B. Weksler, B. Brodin, In vitro models of the blood-brain barrier: An overview of commonly used brain endothelial cell culture models and guidelines for their use, J. Cereb. Blood Flow Metab. 36 (2015) 862–890, doi:10.1177/0271678X16630991.
[67] B. Dehouck, M.P. Dehouck, J.C. Fruchart, R. Cecchelli, Upregulation of the low density lipoprotein receptor at the blood-brain barrier: Intercommunications between brain capillary endothelial cells and astrocytes, J. Cell Biol. 126 (1994) 465–473, doi:10.1083/jcb.126.2.465.
[68] R. Villalonga-Planells, L. Coll-Mulet, F. Martínez-Soler, E. Castaño, J.J. Acebes,

P. Giménez-Bonafé, J. Gil, A. Tortosa, Activation of p53 by nutlin-3a induces apoptosis and cellular senescence in human glioblastoma multiforme, PLoS One 6 (2011) 18588, doi:10.1371/journal.pone.0018588.
[69] E. Fröhlich, The role of surface charge in cellular uptake and cytotoxicity of medical nanoparticles, Int. J. Nanomed. 7 (2012) 5577–5591, doi:10.2147/IJN.S36111.
[70] C.A. Buckner, A.L. Buckner, S.A. Koren, M.A. Persinger, R.M. Lafrenie, Inhibition of cancer cell growth by exposure to a specific time-Varying electromagnetic field involves T-Type calcium channels, PLoS One 10 (2015), doi:10.1371/journal.pone.0124136.
[71] M. Martínez-Carmona, D. Lozano, M. Colilla, M. Vallet-Regí, Lectin-conjugated pH-responsive mesoporous silica nanoparticles for targeted bone cancer treatment, Acta Biomater. 65 (2018) 393–404, doi:10.1016/j.actbio.2017.11.007.
[72] M. Mak, F. Spill, R.D. Kamm, M.H. Zaman, Single-cell migration in complex microenvironments: mechanics and signaling dynamics, J. Biomech. Eng. 138 (2016).
[73] J. Pijuan, C. Barceló, O. Maiques, D.F. Moreno, P. Sisó, R.M. Marti, A. Macià, A. Panosa, In vitro cell migration, invasion and adhesion assays: from cell imaging to data analysis, Front. Cell Dev. Biol. 7 (2019) 107.
[74] S. Tojkander, G. Gateva, P. Lappalainen, Actin stress fibers–assembly, dynamics and biological roles, J. Cell Sci. 125 (2012) 1855–1864.
[75] S.H. Lee, R. Dominguez, Regulation of actin cytoskeleton dynamics in cells, Mol. Cells. 29 (2010) 311–325, doi:10.1007/s10059-010-0053-8.
[76] B.H. Sung, X. Zhu, I. Kaverina, A.M. Weaver, Cortactin controls cell motility and lamellipodial dynamics by regulating ECM secretion, Curr. Biol. 21 (2011) 1460–1469.
[77] T. Ma, Z. Zhang, Y. Lu, Y. Zhang, D. Tao, Y. Liu, Y. Ma, CLOCK and BMAL1 stabilize and activate RHOA to promote F-actin formation in cancer cells, Exp. Mol. Med. 50 (2018) 1–15.
[78] M. Hou, X. Liu, J. Cao, B. Chen, SEPT7 overexpression inhibits glioma cell migration by targeting the actin cytoskeleton pathway, Oncol. Rep. 35 (2016) 2003–2010.
[79] D.M. Moran, C.G. Maki, Nutlin-3a induces cytoskeletal rearrangement and inhibits the migration and invasion capacity of p53 wild-type cancer cells, Mol. Cancer Ther. 9 (2010) 895–905, doi:10.1158/1535-7163.MCT-09-1220.
[80] W. Hui, S. Liu, J. Zheng, Z. Fang, Q. Ding, C. Feng, Nutlin-3a as a novel anticancer agent for adrenocortical carcinoma with CTNNB1 mutation, Cancer Med 7 (2018) 1440–1449, doi:10.1002/cam4.1431.
[81] Q. Wu, X. Wang, J. Liu, J. Zheng, Y. Liu, Y. Li, F. Su, W. Ou, R. Wang, Nutlin-3 reverses the epithelial-mesenchymal transition in gemcitabine-resistant hepatocellular carcinoma cells, Oncol. Rep. 36 (2016) 1325–1332, doi:10.3892/or.2016.4920.
[82] A. Hatoum, R. Mohammed, O. Zakieh, The unique invasiveness of glioblastoma and possible drug targets on extracellular matrix, Cancer Manag. Res. 11 (2019) 1843–1855, doi:10.2147/CMAR.S186142.
[83] I. Restall, D.A. Bozek, C. Chesnelong, S. Weiss, H.A. Luchman, Live-Cell Imaging Assays to Study Glioblastoma Brain Tumor Stem Cell Migration and Invasion, J. Vis. Exp. (2018) 58152, doi:10.3791/58152.
[84] M. Solinas, P. Massi, V. Cinquina, M. Valenti, D. Bolognini, M. Gariboldi, E. Monti, T. Rubino, D. Parolaro, Cannabidiol, a non-psychoactive cannabinoid compound, inhibits proliferation and invasion in U87-MG and T98G glioma cells through a multitarget effect, PLoS One 8 (2013) e76918.
[85] S. Hirohashi, Inactivation of the E-cadherin-mediated cell adhesion system in human cancers, Am. J. Pathol. 153 (1998) 333–339, doi:10.1016/S0002-9440(10)65575-7.
[86] Y. Iwadate, Epithelial-mesenchymal transition in glioblastoma progression, Oncol. Lett. 11 (2016) 1615–1620, doi:10.3892/ol.2016.4113.